



Seismicity along the Santorini-Amorgos zone and its relationship with active tectonics and fluid distribution

R. Andinisari^{a,*}, K.I. Konstantinou^a, P. Ranjan^{a,b}

^a Department of Earth Sciences, National Central University, Chungli, Taoyuan, Taiwan

^b Taiwan International Graduate Program–Earth System Science (TIGP–ESS), Taiwan

ARTICLE INFO

Keywords:

Aegean
Seismotectonics
Santorini
Relocation
Vp/Vs ratio
Seismic hazard

ABSTRACT

The Santorini-Amorgos zone is located in the central part of the Hellenic volcanic arc and is hosting eight large faults as well as Kolumbo and Santorini volcanic centers. The largest earthquake ($M_w \sim 7.1$) in the southern Aegean during the 20th century also occurred in this area on 9 July 1956. A total of 1868 crustal events were recorded by temporary networks during September 2002 to July 2004 and October 2005 to March 2007, and also by the permanent network from 2011 to 2019. We relocated 1455 of these events by using HypoDD and revealed clusters of earthquakes beneath Kolumbo, Anydros graben, and Santorini-Amorgos ridge. Only the faults in the SW of Anydros, SE of Ios, and along the south coast of Amorgos were delineated by the relocated events. Nearly vertical clusters were observed beneath the island of Anydros, south of Amorgos, and in NE end of Amorgos fault, indicating possible pathways of upward migrating fluids. The seismogenic layer thickness calculated based on the depth distribution of the relocated events was 12.5 km. We combined this thickness with geometrical properties of the faults to calculate the expected moment magnitude of future earthquakes, resulting in a range of 6.3–7.2. In an effort to map the distribution of fluids, the Vp/Vs ratio distribution was estimated by utilizing the event-station travel time data along with crack density, fluid saturation, and Poisson's ratio. The petrophysical parameters observed in the northern part of the Santorini caldera suggest the existence of melt, while those observed in Anydros and in the NE of Amorgos fault support the suggestion of upward migrating fluids in these areas.

1. Introduction

The Hellenic subduction zone is an area with high seismicity that was formed by the subduction of the African plate beneath the Aegean at a rate of about 0.9 cm/year (Reilinger et al., 2006; McClusky et al., 2000). This subduction also resulted in the formation of the volcanic centers shown in Fig. 1. About 25 Ma ago during Oligo-Miocene time, the rollback of the African lithosphere initiated the southward migration of the Aegean plate (McClusky et al., 2000). Later in the Miocene, the northward moving Arabian plate collided with the Anatolian plate, resulting in the westward extrusion of the latter. This changed the pure southward migration of the Aegean plate into southwestward direction at a rate of 3.5 cm/year (Le Pichon et al., 1995; Hollenstein et al., 2008; Nyst and Thatcher, 2004; Reilinger et al., 2006; Rontogianni, 2010). Due to the slab rollback of the African lithosphere, gravitational spreading was also initiated causing the present-day extensional deformation of the Aegean plate (e.g., Konstantinou et al., 2016).

In general, the Santorini-Amorgos zone is the boundary between the western Hellenic arc and the more seismically active eastern arc. This zone also exhibits the highest level of seismicity in the Hellenic volcanic arc (Bohnhoff et al., 2006). The seismicity was mainly observed between Santorini and the island of Amorgos as well as in the area between Paros and Naxos islands. Moderate to large earthquakes with $M_w > 5.0$ have also occurred in Santorini-Amorgos zone since the year 1911 up until now (Table 1). The largest among these earthquakes are the two events that occurred on 9 July 1956 at 03:11 UTC and 03:24 UTC, which will be referred to as the 1956 twin earthquakes hereafter. These earthquakes had surface wave magnitudes of 7.4 and 7.3 according to Makropoulos et al. (1999) and also generated a tsunami affecting an extensive area from SE of Amorgos and its surrounding islands up to the Turkish coast (Makropoulos et al., 1999; Papazachos et al., 1985; Perissoratis and Papadopoulos, 1999; Brüstle et al., 2014; Konstantinou, 2010). As many as 53 people were killed, 100 people were injured, and more than 3200 buildings were heavily damaged by both earthquakes (Ambraseys,

* Corresponding author.

E-mail address: ratriandini@ncu.edu.tw (R. Andinisari).

<https://doi.org/10.1016/j.pepi.2021.106660>

Received 5 June 2020; Received in revised form 13 October 2020; Accepted 1 February 2021

Available online 4 February 2021

0031-9201/© 2021 Elsevier B.V. All rights reserved.

1960). Although these events have been extensively studied, their epicenters and hypocentral depths have not been estimated with certainty (earthquakes no. 3 and 4 in Table 1). Multiple studies suggested a SE dipping normal fault as the one responsible for the nucleation of the first event (Comninakis and Papazachos, 1986; Makropoulos et al., 1999; Okal et al., 2009; Brüstle et al., 2014; Nomikou et al., 2018). However, not much is known about the second event. This is due to the fact that the surface wave coda of the first event masked the body wave phases of the following one, so that an analysis of the second event is rather difficult to perform (Brüstle et al., 2014). The 1956 twin earthquakes make seismic hazard assessment in this area particularly important since it is likely that such a large earthquake may occur again in the future.

The Santorini-Amorgos zone also hosts Santorini caldera, which produced its largest eruption in the year 1613 BCE (± 13 years), known as the Minoan eruption (Friedrich, 2013). The volcanic activities of Santorini following this eruption were mostly small, effusive, and occurred periodically, forming the small islands of Nea Kameni and Palea Kameni in the center of the caldera (Nomikou et al., 2014). In January 2011, an increase in micro-seismic activities and intra-caldera uplift were detected, marking the onset of an unrest phase. Movement of magma from the dacitic magma reservoir (depth of 10–14 km) to a shallower rhyolitic magma chamber might have been the cause of this unrest. The magma flow increased the stresses within the upper crust and resulted in the observed seismicity and inflation (Konstantinou et al., 2013; Parks et al., 2015; Druitt et al., 2019). The source of the inflation was most likely located beneath the northern part of the caldera which corresponds to a shallow rhyolitic magma chamber (Newman et al., 2012; Hooft et al., 2019). The seismicity and deformation ceased after 16 months and marked the end of the 2011–2012 unrest without any eruption. About 7 km NE of Santorini, 19 volcanic craters can be observed with NE-SW orientation (Nomikou et al., 2012). The largest crater is known as Kolombo submarine volcano and its last eruption occurred on 29 September 1650 CE. Although located in close proximity to each other, the magmatic systems beneath Santorini and

Kolombo have different mineralogical and geochemical properties. Hence, it is most likely that these volcanic centers have a different magmatic source (Klaver et al., 2016). Considering that the Santorini-Amorgos zone is a volcanic area dominated by extensional deformation similar to the whole Aegean region (Rontogianni, 2010; Reilinger et al., 2006), its crust is most likely pervaded by numerous faults and cracks, allowing magmatic fluids to ascend to the surface or to localize at a certain depth (Heath et al., 2019).

In this work, we utilize a wealth of seismological data recorded by both temporary and permanent networks in an effort to elucidate the following points: (1) the distribution of seismicity with respect to the mapped active faults and the expected moment magnitude of earthquakes they may produce, (2) what role fluids may be playing in the tectonic-magmatic processes in the region. First, we performed absolute and relative location of crustal events recorded by the temporary networks deployed in the southern Aegean as well as the ones that occurred during the last 9 years and were recorded by the permanent network. We then combined the obtained precise relative locations with the active faults in the GREdaSS database (Caputo and Pavlides, 2013), the seismic reflection profiles of Perissoratis and Papadopoulos (1999) and Nomikou et al. (2012, 2016, 2018). We also calculated the thickness of the seismogenic layer and combined it with the geometrical properties of the faults to estimate the expected moment magnitudes of future earthquakes. Our results show that the width of the seismogenic fault is a critical parameter in estimating potential earthquake magnitudes. Finally, we estimated the distribution of the V_p/V_s ratios which allows crack density and fluid saturation to be determined along the study area. These estimates are new for this area and provide the means to understand the relationship between seismicity and upward migrating fluids.

2. Data

Both temporary and permanent seismic networks have been deployed to monitor the seismic activity in the southern Aegean. These

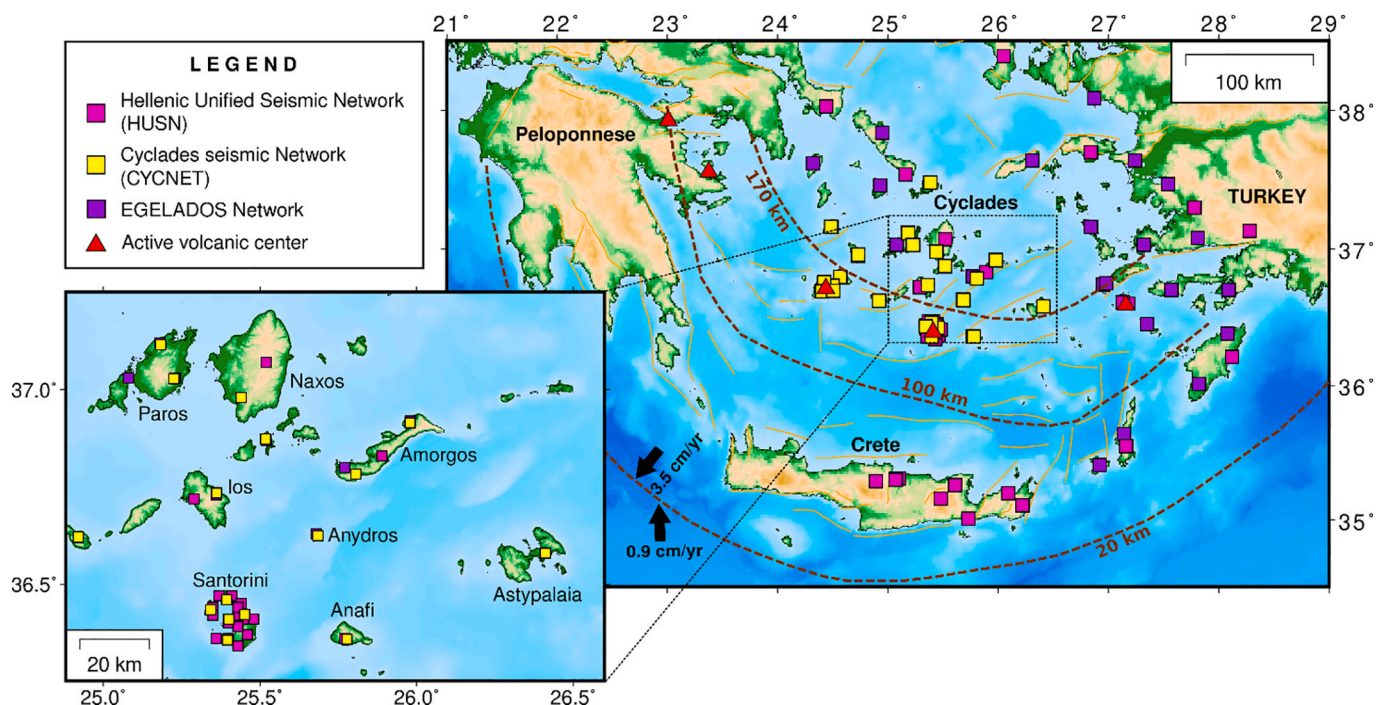


Fig. 1. Map showing the area of the south Aegean. The black arrows represent the present-day plate motions. Dashed brown lines represent isodepth curves of earthquake hypocenters that occurred along the Wadati-Benioff zone (Papazachos et al., 2000). Colored squares indicate stations of the seismic networks listed in the legend. Solid yellow lines represent faults contained in the GREdaSS database (Caputo and Pavlides, 2013). The study area is highlighted by the dashed square and plotted in detail in the bottom left corner inset. (For interpretation of the references to colour in this figure legend, the reader is referred to the web version of this article.)

seismic networks are CYCNET (Cyclades seismic Network) (Bohnhoff et al., 2004), EGELADOS (Exploring the Geodynamics of Subducted Lithosphere Using an Amphibian Deployment of Seismographs) (Friederich and Meier, 2005), and the Hellenic Unified Seismic Network (HUSN). CYCNET was installed on the Cyclades island group for about 2 years starting in September 2002 to July 2004 to monitor microseismic activity of the central Hellenic volcanic arc. It consisted of 22 stations in total with 16 stations equipped with three-component short-period sensors (1-Hz MARK 4 L-3C) and 6 stations equipped with broadband three-component seismometers (STS-2). In October 2005 to March 2007, EGELADOS was deployed with up to 56 stations distributed from the Peloponnese to SW Turkey. All these stations were equipped with three-components sensors (45 Güralp 50-s, 4 STS-2, and 7 1-Hz MARK). Seven permanent broadband seismographs of the GeoForschungsNetz (GEOFON) network and one Mediterranean Very Broadband Seismographic Network (MedNet) station were also included into EGELADOS. We also used events recorded by HUSN which consists of 153 stations equipped with 30–120-s three component broadband seismometers (CMG-3ESPC, CMG-3 T, CMG-40 T, STS-1, STS-2, Le-3D, KS2000M, and TRILLIUM-120p).

We selected shallow crustal events in the Santorini-Amorgos zone that were recorded by CYCNET and EGELADOS during each of their active period. After manual P and S-phase picking was performed for all of these events, we further selected good quality events with 8 or more observed phases of which at least 2 were S-phases. As many as 517 events recorded by CYCNET and 572 events recorded by EGELADOS conformed to these criteria. Based on the catalog of the National Observatory of Athens (NOA), the largest among these events had a local magnitude of 4.1. At this point, it has to be noted that we did not calculate the magnitude of events recorded by CYCNET and EGELADOS.

The events recorded by HUSN are relayed to NOA in order to be manually picked and located. Considering that HUSN was continuously upgraded during its establishment from 2008 to 2011, we focus our study on crustal events recorded from January 2011 to December 2019 when the data quality was the highest. Similarly, with the selection criteria mentioned previously, we searched HUSN data for crustal events that occurred in our study area with 8 or more observed phases of which at least 2 are S-phases. This search yielded as many as 779 events with local magnitudes ranging from 0.8 to 4.6. In this way we selected a total number of 1868 crustal events that occurred along the Santorini-Amorgos zone which is more than the total number of events utilized by Bohnhoff et al. (2006) in a previous study of this region.

Table 1

Source parameters of moderate to large earthquakes with moment magnitude larger than 5.0 in the Santorini-Amorgos zone from the year 1911 to present. OT is the origin time of each earthquake. The letter “f” next to the value of the hypocentral depth indicates that the hypocentral depth was fixed. M and ΔM are the estimated magnitude and the magnitude uncertainty for each earthquake.

No.	Date	OT (UTC)	Lat (° N)	Lon (° E)	H (km)	M	ΔM	Reference
1	04-04-1911	15:43:48.98	36.52	25.74	15f	6.07 M_w	0.20	ISC-GEM
2	25-10-1919	17:10:07.23	36.51	25.87	15f	6.03 M_w	0.41	ISC-GEM
3	09-07-1956	03:11:45.15	36.66	25.96	25	7.70 M_w	0.20	ISC-GEM
		03:11:40	36.70	25.80	< 70	7.5 M_s	-	Comninakis and Papazachos (1986)
		03:11:43.7	36.64	25.92	15	7.4 M_s	-	Makropoulos et al. (1999)(Ambraseys, 2001)
		03:11	36.72	25.51	15	7.18 M_s	-	
		03:11:45	36.72	25.76	45	7.69 M_w	-	Okal et al. (2009)
		03:11	-	-	25	7.1 M_w	-	Brüstle et al. (2014)
4	09-07-1956	03:24:05.74	36.39	25.87	15f	-	-	ISC-GEM
		03:24:03	36.45	25.51	< 70	6.9 M_s	-	Comninakis and Papazachos (1986)
		03:24:16.5	36.45	25.51	95	7.2 M_s	-	Makropoulos et al. (1999)
		03:24	36.65	25.80	30	6.00 M_s	-	(Ambraseys, 2001)
		03:24:07	36.39	25.78	-	-	-	Okal et al. (2009)
		03:24	-	-	> 100	-	-	Brüstle et al. (2014)
5	09-07-1956	06:22:49.99	36.62	25.79	15f	5.47 M_w	0.20	ISC-GEM
6	09-07-1956	20:13:57.29	36.83	26.16	15f	5.50 M_w	0.23	ISC-GEM
7	10-07-1956	03:01:29.24	36.69	26.21	15f	5.65 M_w	0.32	ISC-GEM

3. Earthquake relocation

Absolute location of all the picked events was performed by using the probabilistic nonlinear algorithm NonLinLoc (Lomax et al., 2000). Before absolute locations can be estimated, theoretical travel times for every station were calculated by utilizing a 3D grid of $400 \times 400 \times 160$ cells with $1 \times 1 \times 1$ km spacing. The finite difference algorithm of Podvin and Lecomte (1991) and the 1D velocity model of Brüstle (2012) (Table 2) were employed to perform this calculation. This velocity model was inverted from well-located events recorded by EGELADOS, therefore it was considered suitable for this study. Since the mentioned velocity model does not include station delays, we performed the absolute location in two stages. In the first stage, we obtained average residuals of both P and S-wave arrivals for all the stations. These residuals were then used as station delays in the second stage where final absolute locations were obtained. The horizontal (ERH) and vertical uncertainties (ERV) for the final absolute locations were later calculated based on the diagonal elements of the covariance matrix of each event (Maleki et al., 2013). The value of each element contained in the covariance matrix depends on the shape of the posterior density function, therefore an irregular shape will result in high ERH and ERV values.

The absolute locations of all the crustal events located in Santorini-Amorgos zone are shown in Fig. 2. A large number of crustal earthquakes can be observed in concentrated clusters extending from NE of Santorini to the south of Amorgos in NE-SW orientation. Prominent seismicity can also be found in the north to NE of Astypalaia, albeit less in number and less clustered. Aside from that, a smaller cluster consisting of tens of shallow earthquakes with depth less than 10 km appears in between the islands of Paros and Naxos. The average RMS residual of all the absolute locations is equal to 0.26 s (± 0.29 s) with the

Table 2

P and S-wave velocity model of Brüstle (2012) used to obtain absolute and relative locations of all the crustal events in this study.

Depth (km)	P-velocity (km/s)	S-velocity (km/s)
< 5	5.74	3.08
5–10	5.89	3.38
10–15	5.89	3.45
15–20	5.91	3.45
20–25	6.23	3.77
25–30	6.26	3.93
30–35	7.53	4.10
35–40	7.55	4.10

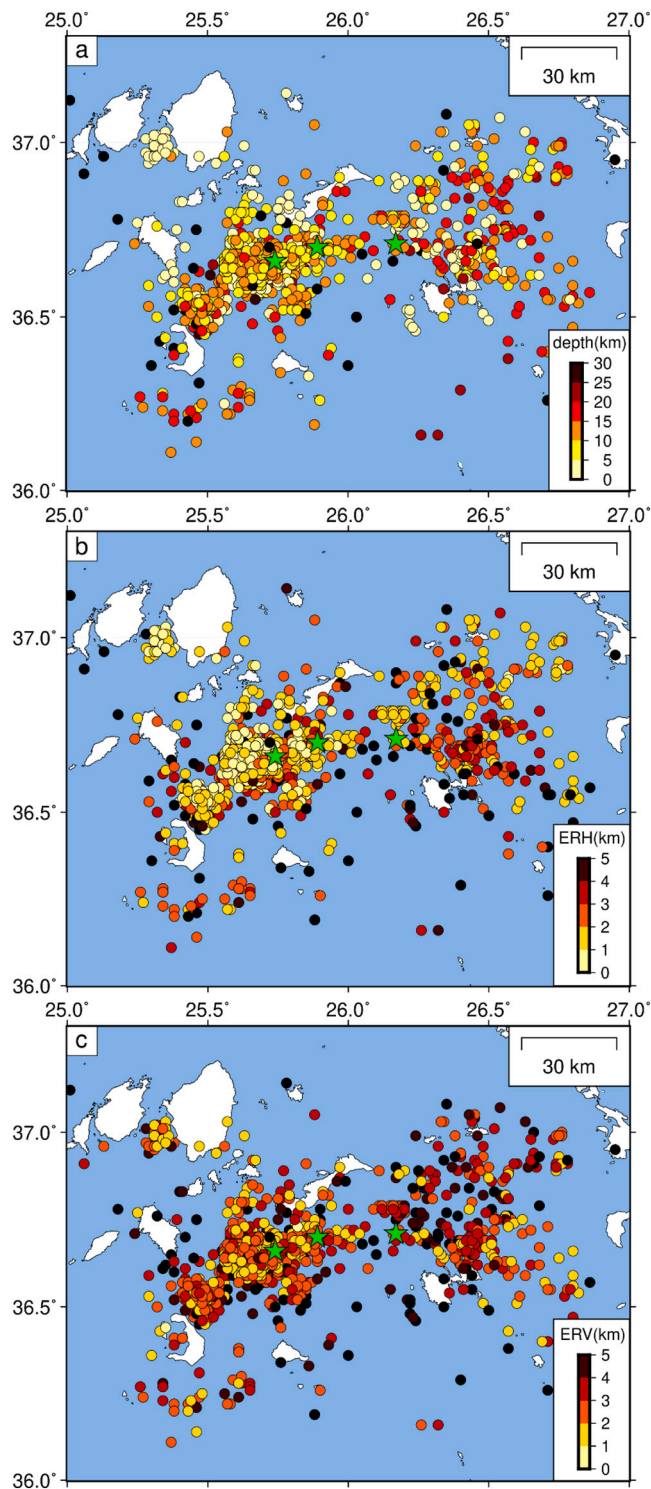


Fig. 2. Absolute locations of all the events in the study area plotted based on their (a) hypocentral depths, (b) horizontal uncertainties or ERH, and (c) vertical uncertainties or ERV. Green stars represent the location of moderate earthquakes that occurred during our period of study. (For interpretation of the references to colour in this figure legend, the reader is referred to the web version of this article.)

average ERH and ERV of $2.3 \text{ km} (\pm 5.2 \text{ km})$ and $3.1 \text{ km} (\pm 2.2 \text{ km})$, respectively. The distributions of RMS residuals, ERH, and ERV of all the absolute locations can be found in Fig. S1 in the Supplementary Material. Events with small ERH are the ones distributed from the NE of Santorini to the south of Amorgos and the ones located between Paros

and Naxos. The ERH of the events in the north of Astypalaia are generally larger due to the fact that the closest stations in this area are located 30 km away. Aside from that, these events also have large azimuthal gaps. In general, the ERH of events located in the western part of Santorini-Amorgos zone are smaller than the ones located in the eastern part. A similar trend can also be observed for ERV, even though the discrepancy of ERV between the western and eastern parts is smaller.

In order to improve the resolution of hypocenters, relative locations were obtained by using the double-difference algorithm, or HypoDD, of Waldhauser and Ellsworth (2000). The relocation can be performed by using either catalog or both catalog and waveform cross-correlation differential times of P and S-waves that we obtained from all of our datasets. In this study, we applied a separation distance of 15 km for stations up to 200 km away from the source. To improve connectivity between events, each of them was required to have at least 10 neighbors. As many as 1632 events were obtained by this parameterization, with the total of 277,518 P-phases and 173,120 S-phases. The constructed chain of events has an average number of links per event pair of 10 and average offset between events of 5.2 km. There were 4% of phase outliers and 17% of weakly linked events, which means that the catalog data has relatively good quality and exhibit tight clustering.

Differential times from waveform cross-correlation of P and S-phases with correlation coefficient higher than 0.7 were used along with catalog data to increase the precision of the relative locations. We first lowpass-filtered the waveforms with a corner frequency of 5 Hz and then cross-correlated them by using a window length of 2 s for P-phases and 3 s for S-phases.

Seismic waves with higher frequencies tend to undergo strong scattering as observed across the southern Aegean by Ranjan et al. (2019). Scattering in high frequencies is expected to deteriorate the similarity between waveforms. In order to confirm this, we also bandpass-filtered the waveforms with a bandwidth of 1–10 Hz. We found that the 5 Hz lowpass-filter produced 134,734 P and 38,222 S-pairs with correlation coefficient larger than 0.7, while the bandpass-filter with 1–10 Hz bandwidth only produced as many as 25,756 P and 4676 S-pairs (Fig. S2 in the Supplementary Material). All waveform cross-correlations were performed by using a modified version of the multi-channel cross-correlation method of VanDecar and Crosson (1990). Finally, relative relocation was carried out by utilizing the minimum 1D velocity model of Brüstle (2012) and a V_p/V_s ratio of 1.70. The V_p/V_s ratio was calculated by using a Wadati diagram of P-arrivals and S–P travel time differences of events with hypocentral depth of less than 25 km (Fig. S3 in the Supplementary Material).

The relative relocation problem was solved by using the LSQR conjugate gradients method as it is more efficient for large datasets. We set the damping parameter to 95 to obtain condition numbers of 40 to 80 for most of the earthquake clusters as suggested by Waldhauser (2001). Higher a priori phase weightings were given to the catalog data in the first five iterations to ensure that the relative locations of all events were obtained. The catalog data were later down-weighted relative to the cross-correlation data in the next five iterations. This was done to improve the locations of event pairs with small separation distances and also to remove possible outliers. As many as 1455 events ($\sim 78\%$) were relocated with average RMS residual of $0.06 \text{ s} (\pm 0.13 \text{ s})$ which is lower than the average RMS residual of absolute locations from the previous section (0.26 s). Even though the LSQR method is efficient and suitable for our dataset, it does not produce accurate location uncertainties. Therefore, we estimated the uncertainties by relocating smaller earthquake clusters with the Singular Value Decomposition (SVD) method (Waldhauser, 2001). Four small earthquake clusters with detailed information displayed in Table 3 were chosen, resulting in maximum horizontal and vertical uncertainties of 0.16 km and 0.28 km, respectively. The catalog of relative locations for all the events is provided in Table S1 in the Supplementary Material. In the next section, we will discuss the features of the relocated events and present cross-sections in order to examine their relationship with several imaged faults in the

Table 3

The results of smaller earthquake clusters relocation by using SVD in order to obtain reliable relative relocation uncertainties. The number of events in each cluster is represented by N; the centroid location of each cluster is represented by cLat, cLon, and cH; the mean uncertainties are represented by ErrX ErrY ErrZ.

ID	N	cLat(°)	cLon(°)	cH(km)	ErrX(km)	ErrY(km)	ErrZ(km)
1	242	36.64	25.61	8.84	0.16	0.11	0.28
2	235	36.53	25.50	8.92	0.09	0.08	0.28
3	217	36.63	25.69	8.84	0.11	0.08	0.20
4	42	36.78	26.17	11.51	0.09	0.10	0.28

area.

4. Seismicity distribution

The obtained relative locations are plotted in Fig. 3 along with moment tensor solutions provided by NOA (Konstantinou et al., 2010) and mapped fault traces. These faults are the Santorini-Anafi Fault (SAF), Amorgos Fault (AmF), smaller secondary faults, such as Anafi Fault (AnF) and West Astypalaea Fault (WAsF), as well as two fault clusters namely Ios Fault (IF) and Anydros Fault (AF) (Sakellariou et al., 2010; Nomikou et al., 2012, 2016, 2018). The relocated events are mainly concentrated beneath Kolumbo submarine volcano, as well as in the Anydros graben and along the Santorini-Amorgos ridge. Smaller earthquake clusters can also be observed between the islands of Paros and Naxos, between Amorgos and Astypalaea, as well as in the north to NE of Astypalaea. Similar spatial distribution of crustal events in Santorini-Amorgos zone was also observed by Bohnhoff et al. (2006). It

is important to note that the locations of earthquakes that occurred on 10 April 2018 and 27 November 2018 were not relocated by HypoDD, as these became weakly linked. Instead, the locations of both earthquakes plotted in Fig. 3 are the absolute locations calculated by using NonLinLoc.

The earthquake cluster beneath Kolumbo is located about 5 to 10 km NE of Santorini. The Kolumbo volcanic chain itself consists of at least 19 dome-shaped and cratered structures with NE and NNE principal trends as shown in Fig. 4. A small number of events of this cluster is located around volcanic craters (VC) 2, 3, 4, and 6, indicating that the NE trend of the volcanic craters is more active compared to the westerly trend. Similar observations were also reported by Nomikou et al. (2012) who examined swath bathymetry and rock samples in the area. The hypocentral depths of the events in the aforementioned cluster are less than 19 km with most events concentrated between the depth of 8–16 km (Fig. 5). The observed depth distribution of the mentioned cluster is slightly deeper compared to the results of Bohnhoff et al. (2006) and Dimitriadis et al. (2009) where events are concentrated between 6 and 12 km and 6–9 km, respectively.

The cluster beneath Kolumbo is located in close proximity to the south-western end of AF, so that the fault plane of AF should have been visible in cross-sections d-d' to f-f' of Fig. 5. However, our result in cross-sections d-d' and f-f' do not reveal any fault structure. The only cross-section that shows NW dipping fault plane which could coincide with AF is e-e'. This indicates that the earthquake cluster beneath Kolumbo may not be caused solely by the mentioned fault. Seismic tomography performed by Dimitriadis et al. (2010) indicates that a magma chamber may exist at depths of 6–7 km (inset in cross-section g-g' of Fig. 5) where

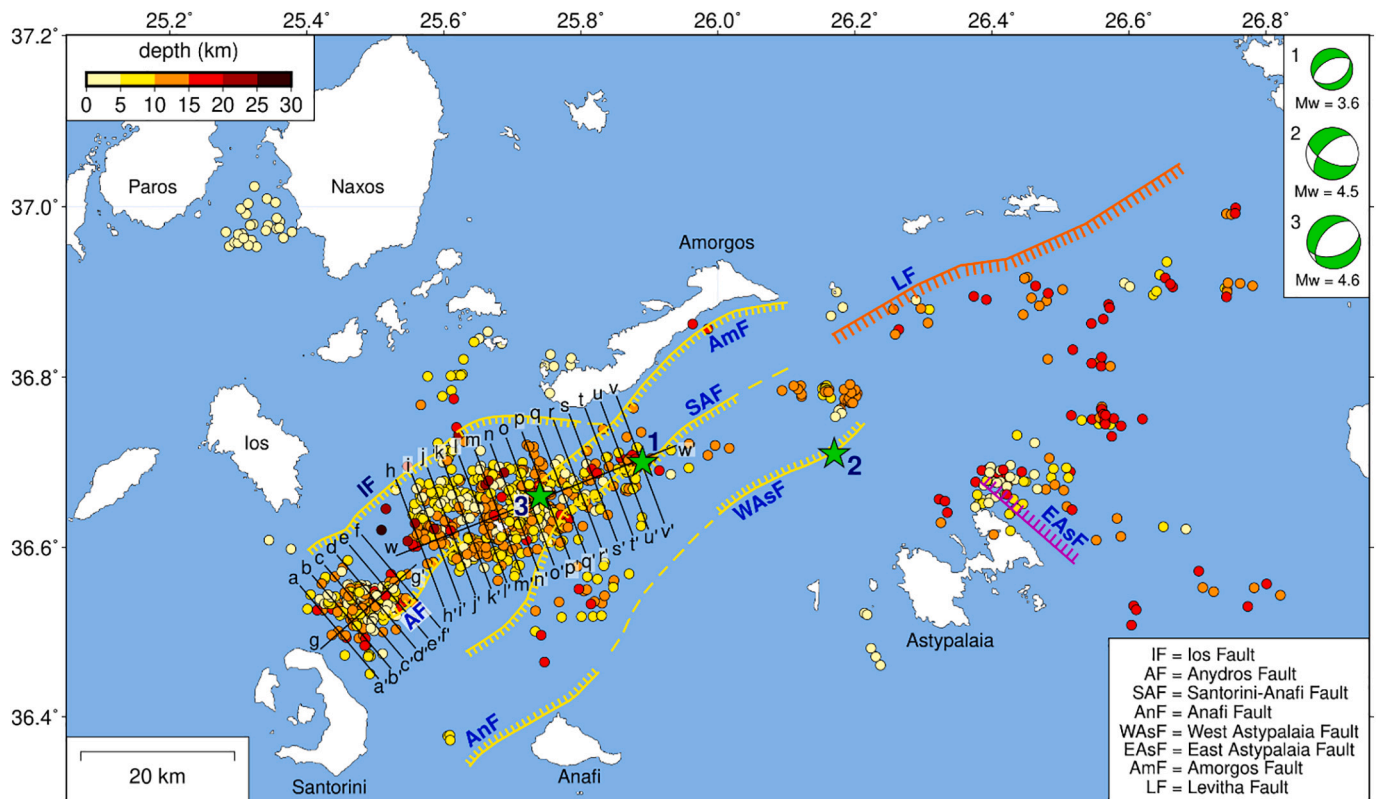


Fig. 3. Relative locations of all the events in the Santorini-Amorgos zone and its surrounding area. The colour of every circle represents a depth value based on the scale at the upper left. Yellow lines indicate major faults in the Santorini-Amorgos zone investigated by Nomikou et al. (2018). Magenta line indicates a fault imaged by Perissoratis and Papadopoulos (1999) and the orange line represents a fault contained in GreDaSS database (Caputo and Pavlides, 2013). Green stars represent moderate earthquakes that occurred on (1) 7 November 2012, (2) 10 April 2018, and (3) 27 November 2018, which are included in our period of study. The green beach balls in the upper right corner show focal mechanisms of the mentioned events provided by NOA (Konstantinou et al., 2010). The black lines represent the depth cross-sections shown in the following figures. (For interpretation of the references to colour in this figure legend, the reader is referred to the web version of this article.)

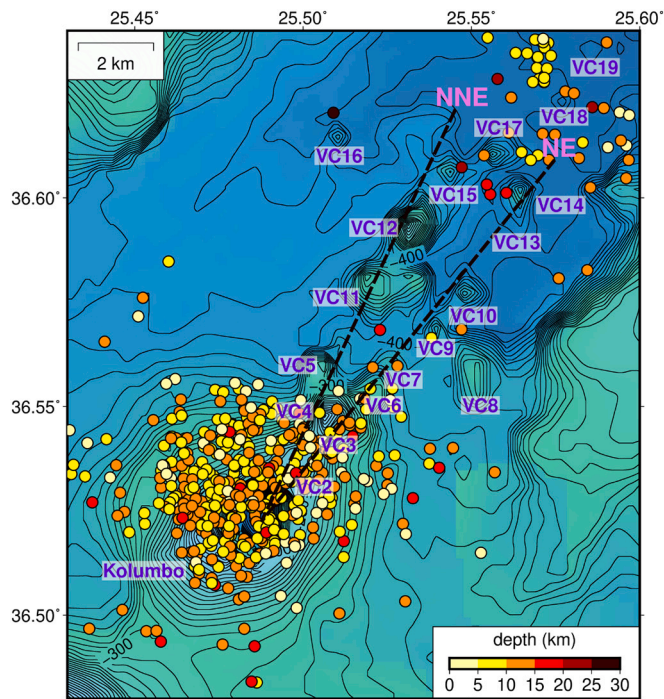


Fig. 4. Distribution of crustal events beneath Kolumbo submarine volcano. Dashed black lines represent the NNE and NE trends of volcanic craters. VC2 to VC19 represent volcanic craters reported by Nomikou et al. (2012). The bathymetry data used in this figure is taken from General Bathymetric Chart of the Oceans (GEBCO) of Weatherall et al. (2015).

there is an area of less seismicity. The lack of seismicity is most likely related to the existence of hot and ductile crust surrounding a melt body. The onset of intense seismic activities can be found directly below the magma chamber. This observation is compatible with the hypocenter distribution of events presented by Dimitriadis et al. (2010). Bohnhoff et al. (2006) suggested that the bulk of seismicity observed beneath Kolumbo was probably related to the accumulation of magma and fluid migration to the surface. However, since most seismicity occurred below the imaged magma chamber, it seems likely that it represents the steady migration of fluids from greater depths to the Kolumbo chamber as also suggested by Konstantinou (2020).

The next prominent cluster in our study area is the NE-SW oriented earthquake cluster along Santorini-Amorgos ridge. The hypocentral depths of events in this cluster vary from 0.8 to 24.4 km and only a small number of them are located at depths greater than 20 km (Fig. 6). The largest earthquakes in this cluster are the ones that occurred on 7 November 2012, 10 April 2018, and 27 November 2018 with moment magnitudes of 3.6, 4.5, and 4.6, respectively. The M_w 4.5 earthquake on 10 April 2018 was not followed by any aftershocks and had no other neighboring events. Similarly, the earthquake on 27 November 2018 is relocated at the depth of 19.8 km and was only followed by another much shallower event (3.9 km). The hypocentral depth of the mentioned earthquake is relatively deeper compared to nearby events (cross-sections p-p' and w-w' in Fig. 6).

The earthquake cluster along Santorini-Amorgos ridge is bounded by IF in the NW and SAF in the SE as well as intersected by AF and AmF (see Fig. 3). However, not all of the mentioned faults can be recognized in cross-sections h-h' to v-v'. The first fault that can be observed from the depth cross-sections is IF. Cross-section j-j' reveals a SE dipping fault which agrees well with the dipping direction of IF as observed by Nomikou et al. (2018). The next fault that can be seen in the depth cross-sections is AmF. Dipping angle of AmF is steep (59° - 66°) along its SW end and is shallower along the SE coast of Amorgos (Nomikou et al., 2018). However, the moment tensor solution of an earthquake on 27

November 2018 (hypocentral depth at 19.8 km) that occurred close to the SW segment of AmF shows a SE dipping fault with a dipping angle of less than 53° (see Fig. 3). These observations are in accordance with cross-sections q-q' and r-r' which reveal that the SW part of AmF has a steeper dipping angle at depths less than 8 km and possibly a shallower dipping angle at greater depths.

Even though the depth cross-sections in Fig. 6 do not show any other fault-like structure except from IF and AmF, the moment tensor solution of earthquake on 7 November 2012 which occurred close to SAF shows a SE dipping angle of 59° (see Fig. 3). This agrees well with the dipping angle of SAF observed in the swath bathymetry data of Nomikou et al. (2012, 2016, 2018). Therefore, it seems likely that the 2012 earthquake ruptured a small segment of SAF. However, instead of exhibiting a fault plane that resembles SAF, the hypocenters of events around the 2012 earthquake exhibit an almost vertical earthquake cluster as shown in cross-section v-v'. Other than this, similar vertical clusters can be observed beneath Anydros as shown in cross-sections m-m' and n-n'. Bohnhoff et al. (2006) also observed such structures in NE end of AmF and interpreted these as local pathways of upward migrating fluids resulting from crustal weakness, or as a sign of emerging volcanic activity, which is commonly found in extensional regimes (Corti et al., 2003).

A smaller and less concentrated earthquake cluster was found in the north to NE of Astypalaia where a similar cluster was also observed by Brüstle (2012). This cluster coincides with a NE dipping normal fault with a NW-SE oriented strike identified in the seismic reflection profiles of Perissoratis and Papadopoulos (1999), which will be referred to as East Astypalaia Fault (EAsF) hereafter. Another small cluster consists of shallow earthquakes with hypocentral depths of less than 10 km can be observed between the islands of Paros and Naxos. This cluster was also observed by both Bohnhoff et al. (2006) and Brüstle (2012). Interestingly, the islands of Paros and Naxos are located in the southern boundary of the Cycladic metamorphic core complex that is mostly aseismic. A small number of earthquakes are relocated east of Amorgos in an almost ENE-WSW orientation. These earthquake locations are very close to the Levitha Fault (LF), a SE to SSE dipping normal fault contained in the GrDaSS database (Caputo and Pavlides, 2013).

5. Active faults and expected moment magnitudes

The first of the 1956 twin earthquakes was the largest earthquake to have occurred in the southern Aegean during the 20th century and may have been caused by one of the faults in the Santorini-Amorgos zone, putting seismic hazard assessment in a place of high importance. A first step towards such an assessment is to estimate the expected earthquake magnitude along each fault in the zone. One of the important parameters in this estimation is the seismogenic layer thickness H , which can be determined from the hypocenter distribution of the relative locations obtained in the previous section. The fault width W can be calculated as $W = H/\sin\delta$, where δ is the dipping angle of a particular fault. The rupture area A is then obtained by multiplying the value of W and the fault length L . The use of both fault length and width gives a more accurate estimate of expected magnitude compared to the use of fault length only. The expected moment magnitudes along the faults in the Santorini-Amorgos zone were then calculated by using the scaling relationships of Konstantinou (2014) for earthquakes in the Mediterranean region that connect moment magnitude M_w with rupture area A as

$$M_w = \log A + 3.82, \text{ if } A \leq 251 \text{ km}^2 \quad (1)$$

$$M_w = \frac{4}{3} \log A + 3.07, \text{ if } A > 251 \text{ km}^2 \quad (2)$$

The seismogenic layer thickness H is determined by subtracting the 5th percentile of the hypocenter distribution from the 95th percentile as shown in Fig. 7. We found the seismogenic layer thickness of the study area to be 12.5 km, which is slightly thinner compared to other areas in

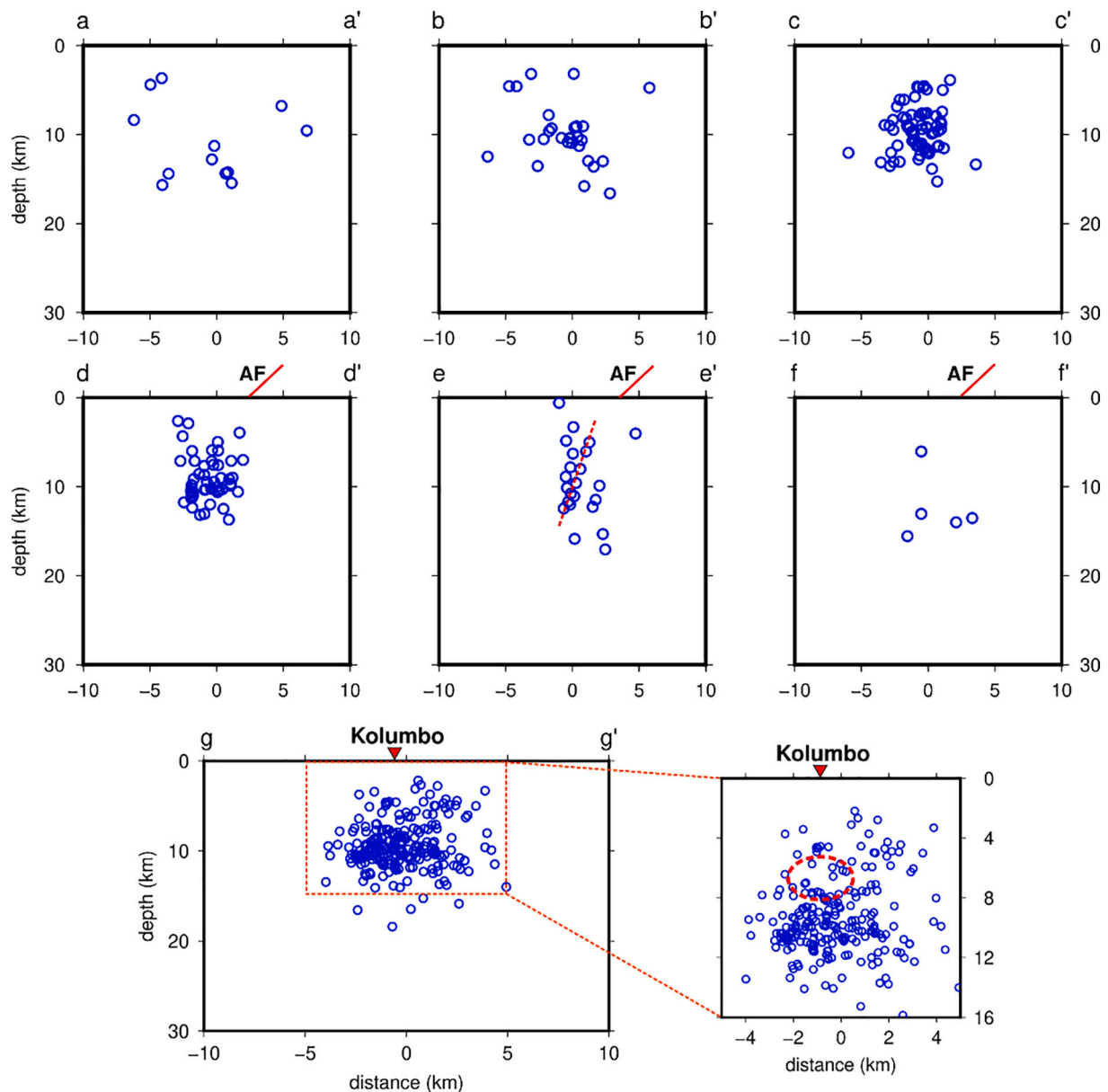


Fig. 5. Depth cross-sections corresponding to the profile shown in Fig. 3. Red lines represent the location and the dip of the major faults in the area according to Nomikou et al. (2018). Dashed red line outlines the orientation of the delineated fault planes. Dashed red ellipse in the inset of cross-section g-g' represents the location of Kolumbo magma chamber according to Dimitriadis et al. (2010). These cross-sections are plotted using a width of 1 km. (For interpretation of the references to colour in this figure legend, the reader is referred to the web version of this article.)

the Aegean. NE and SE Aegean, for instance, have thicker seismogenic layers of 14.8–15.8 km and 12.1–15.4 km respectively (Konstantinou, 2018; Andinisari et al., 2020). It should be noted that the M_w calculated here is the maximum magnitude of future earthquake at each fault since we assume that the fault will rupture along its entire length.

The Santorini-Amorgos zone hosts at least eight faults of which some of them have ruptured in the past, producing earthquakes with moment magnitudes >5.0 . Moderate to large earthquakes along with their error ellipses from the ISC-GEM catalog (Storchak et al., 2013) are shown in Fig. 8 and also listed in Table 1. One of these faults is contained in the GRDaSS database (Caputo and Pavlides, 2013) while the others were imaged in seismic reflection profiles published by Perissoratis and Papadopoulos (1999) and Nomikou et al. (2012, 2016, 2018). These faults are mainly normal faults with NE-SW strike and are located between Santorini and Amorgos (i.e., IF, AmF, AF, SAF, AnF, and WAsF). We also calculated the expected magnitudes along LF, located to the east

of Amorgos, and EAsF which is located NE of Astypalaia. We used the length (L) and dipping angle (δ) of each fault, adopted from the aforementioned studies. Since a single fault may have more than one dipping angle as shown in seismic profiles of Nomikou et al. (2018), we utilized the median of all observed dipping angles in order to calculate the fault width. If any moment tensor solution was available, we also utilized the fault plane dip to calculate seismogenic width along a particular fault. The moment tensor solutions that we used in this study were provided by various agencies, such as NOAA, GFZ (GeoForschungsZentrum), NKUA (National Kapodistrian University of Athens), KOERI (Kandili Observatory and Earthquake Research Institute), and ERD (Earthquake Research Department of Disaster and Emergency Management Presidency of Turkey). Considering that we are using fault dips obtained from the reflection data which most likely imaged only the near-surface part of the faults, it is important to assess the effect of fault dips on the resulting expected magnitudes. Therefore, we also calculated the expected

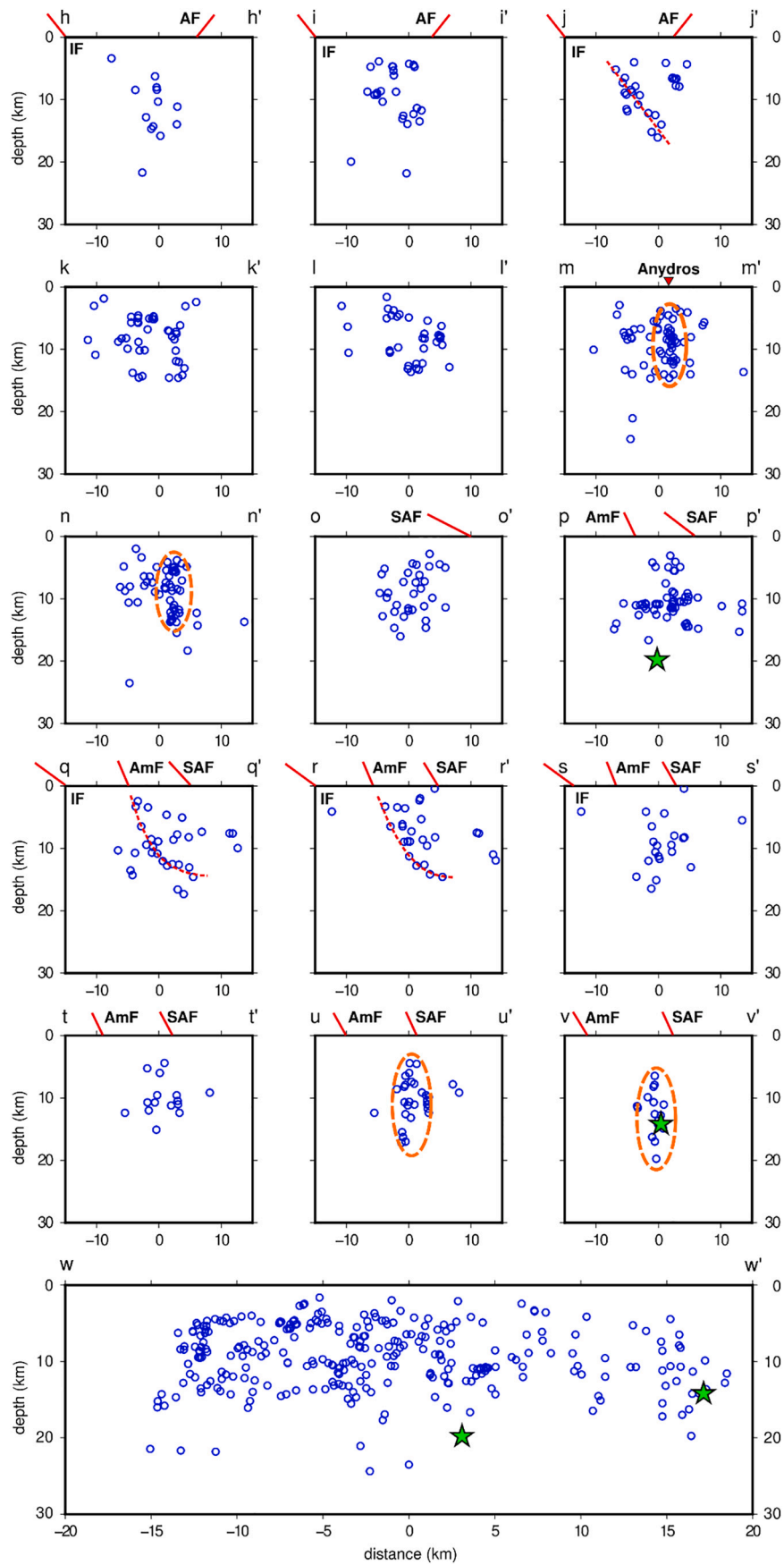


Fig. 6. Same as Fig. 5 for the rest of the depth cross-sections. Other symbols are the same as in Fig. 3. Dashed orange ellipses indicate the locations of vertical event clusters in the area. Each of these cross-sections has a width of 3 km.

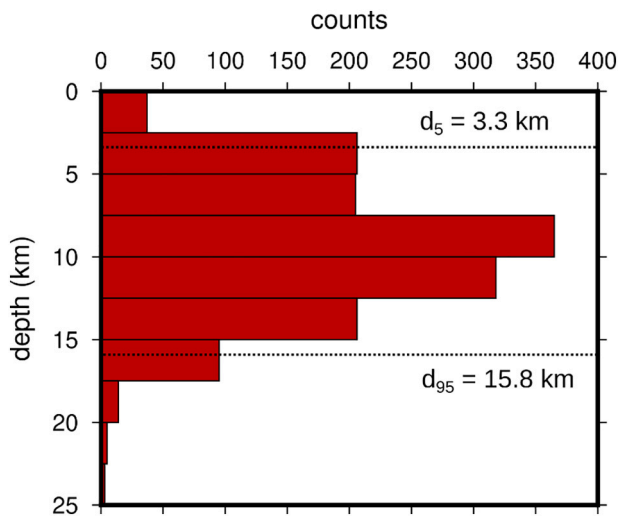


Fig. 7. Histogram with a bin size of 5 km that depicts the hypocentral depth distribution of crustal events beneath the Santorini-Amorgos zone. The d_5 and d_{95} symbols represent 5th and 95th percentiles of the distribution. The seismicogenic layer thickness of the area is the difference between d_5 and d_{95} which is equal to 12.5 km.

magnitudes of all faults in our study area by using the average and maximum fault dips found in normal faults, which are 45° and 60° , respectively (Collettini and Sibson, 2001). These calculations show a difference of 0.1 magnitude unit between expected magnitude calculated by using the average and maximum fault dip as shown in Table S2 in Supplementary Material. Table 4 lists the geometrical properties of each fault along with the resulting expected magnitudes.

5.1. Ios fault (IF) and anydros fault (AF)

IF and AF are the two faults that mark the boundaries of Anydros basin and may also control the volcanic activity of Kolumbo (Sakellariou et al., 2010). IF is a normal fault with NE-SW to E-W strike located north of Santorini to the SW of Amorgos. This fault does not directly coincide with the earthquake cluster beneath Kolumbo volcano, but it is located very close to the earthquake cluster NW of Anydros. The south western part of IF dips to the SE with dipping angle of 53° - 54° while the eastern part dips to the west with low dipping angle of 18° - 37° (Nomikou et al., 2018). There is no event with moment tensor solution that may have been caused by this fault. In order to calculate the expected moment magnitude, we used the median dipping angle of 45° as well as the fault length of 40 km and found a value of 6.9. Located across the south western end of IF, AF is a NW dipping normal fault with a fault dip of less than 50° and fault length of 15–20 km (Nomikou et al., 2012, 2016). Similar to IF, this fault is not associated with any event with moment tensor solution during the different periods covered by of our study. AF is located very close to the Kolumbo submarine volcano and the earthquake cluster beneath it, thus the fault plane can be observed in depth cross section e-e' (Fig. 5). By assuming that AF has a dipping angle of 45° and a maximum length of 20 km, our calculation yielded an expected moment magnitude of 6.5. However, none of the moderate to large earthquakes that occurred in the study area is related to either IF or AF (cf. Fig. 8).

5.2. Amorgos fault (AmF) and Santorini-Amorgos fault (SAF)

AmF is a SE dipping normal fault which is located 5–10 km NE of Anydros and has a total length of 40 km. Swath bathymetry data show that the dipping angle of this fault varies between 38° to 66° with the steepest fault plane located in the south-western segment of the fault (Nomikou et al., 2018). We used the median of these dipping angles

(51°) to calculate the expected moment magnitude along this fault, yielding a value of 6.8. AmF is also the fault that might have caused a moderate earthquake on 27 November 2018 (M_w 4.6) since this event is located exactly in the south-western end of this fault (see Fig. 3). The nodal planes of available moment tensor solutions provided by multiple agencies show that this earthquake exhibited dipping angles between 36° and 53° . By using the length of AmF and taking the median dip of the nodal planes from moment tensor solutions as dipping angle (45°), we obtained an expected moment magnitude of 6.9. Based on cross-sections q-q' and r-r' (Fig. 6), AmF may be a listric normal fault with different dipping angles that correspond to different depths. Therefore, the expected moment magnitude of AmF calculated by using these dipping angles is also considered as a second scenario. According to the mentioned cross-sections, AmF has steeper dipping angle at depths less than 8 km and lower dipping angle at greater depth. We then split the seismicogenic layer thickness into two parts: the shallow part starts at the depth of 3.3 km, which is the onset of the seismicogenic layer (Fig. 7) up to the depth of 8 km, and the deeper part starts at a depth of 8 km down to the depth of 15.8 km. For the shallow part, we used the steepest dipping angle of AmF observed in the seismic profile of Nomikou et al. (2018), which is 66° . As for the deeper part, we used the lowest dipping angle found in moment tensor solutions (36°). The scheme of this calculation is illustrated in the inset of Fig. 8. The rupture areas for the shallow and deeper parts of AmF were calculated and the total rupture area was used to estimate the expected moment magnitude along AmF, resulting again in a value of 6.9.

Similar to AmF, SAF is a SE dipping normal fault with a total fault length of 60 km. This fault marks the NW border of Santorini-Anafi basin with the dipping angles between 28° and 68° as observed by Nomikou et al. (2012, 2016, 2018). Taking the median of these dipping angles (55°), we calculated the expected moment magnitude and found a value of 7.0. Although the fault plane of SAF cannot be observed in any depth cross-sections (see Fig. 6), this fault was probably the one that caused the 4 April 1911 (M_w 6.07 ± 0.20) earthquake. The earthquake that occurred on 7 November 2012 (M_w 3.6) might have been also associated with SAF considering that it was located very close to the central segment of this fault (see Fig. 3). The focal mechanism of the 2012 earthquake, derived by NOA, shows a fault plane with dipping angle of 37° . We then used this dipping angle to calculate the expected moment magnitude of SAF, yielding a value of 7.2.

It is still unclear which fault along the Santorini-Amorgos zone caused the first of the 1956 twin earthquakes. Several studies determined the epicenter of the first event whose location varies from the east of Ios to the south of Amorgos (Fig. 8). However, most of these locations do not have proper error bounds except from that estimated by Okal et al. (2009) and those contained in the ISC-GEM catalog. Okal et al. (2009) located the first of the 1956 twin earthquakes between AF and IF. The uncertainty of this location, however, suggests that the epicenter could lie anywhere from the south-western Amorgos to the SW area of AmF. Meanwhile, ISC-GEM catalog shows that this event occurred in the SE part of SAF. The locations proposed by both studies suggest that the first event might have nucleated at IF, AmF, or SAF. Another critical parameter that has to be taken into account is hypocentral depth. Brüstle et al. (2014) estimated the hypocenter of this event to be at 25 km (± 5 km) depth. Konstantinou (2010) calculated the differential stress of the lithosphere in the area as a function of depth and found that the maximum strength lies at the depth of 33 km. The hypocenter of the first event might also lie at the depth of ~ 33 km since such large earthquakes usually nucleate at the depth of maximum lithospheric strength where peak strain energy is accumulated (Sibson, 1984). Both studies therefore suggest that the first event nucleated at or below the Moho (~ 25 km depth). Since there is no evidence that the aforementioned crustal faults extend down to 25 km depth, it is not possible to conclude with certainty which fault ruptured during the first of the 1956 twin earthquakes.

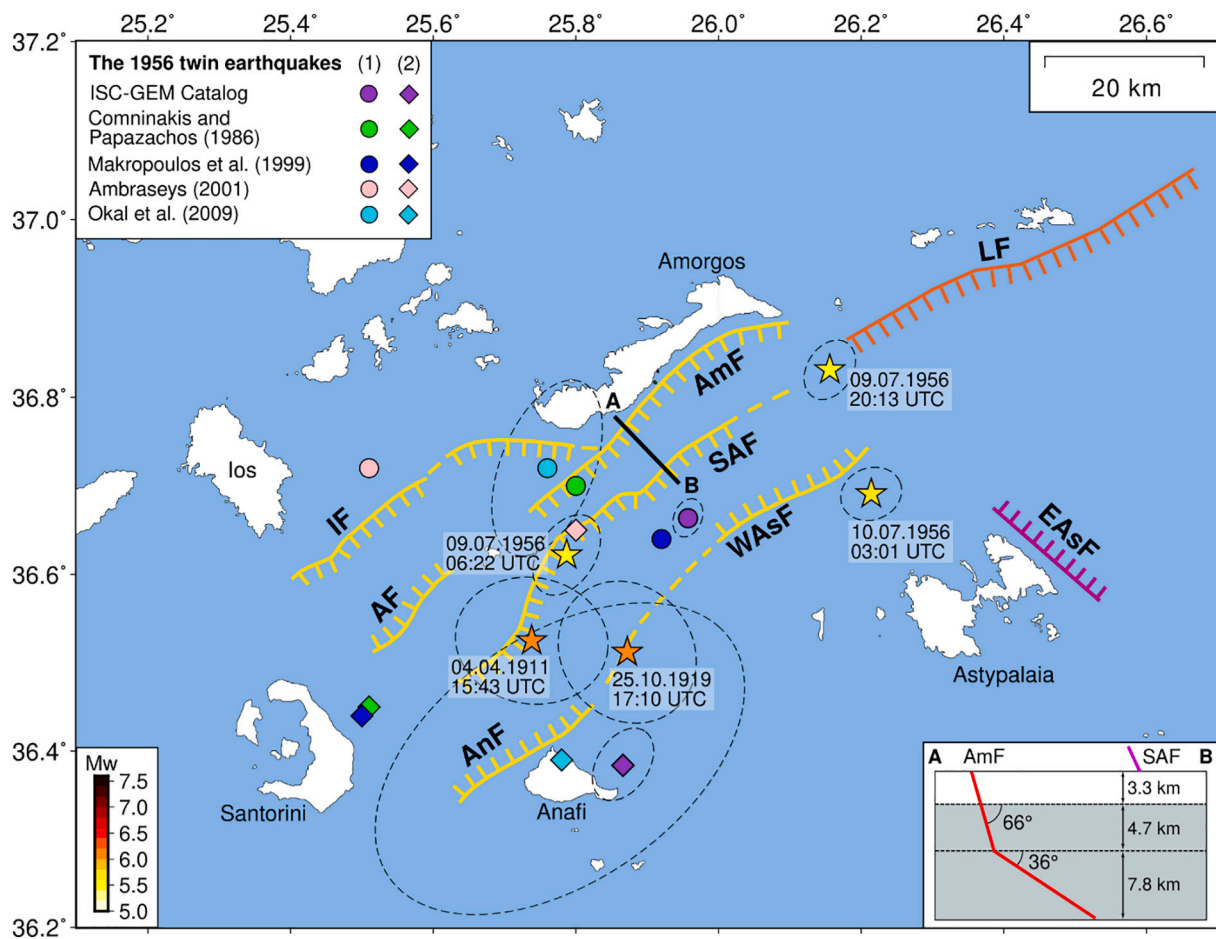


Fig. 8. Map showing the active faults and moderate to large earthquakes that occurred in Santorini-Amorgos zone. The stars represent the locations of the moderate to large events from 1911 to present taken from the ISC-GEM catalog (Storchak et al., 2013). The colour of every star represents moment magnitude based on the scale at the lower left. The dashed ellipses indicate the location uncertainties of the earthquake locations. Colored circles and diamonds represent the locations of the first (9 July 1956, 03:11 UTC) and second event (9 July 1956, 03:24 UTC) of 1956 twin earthquakes contained in ISC-GEM catalog as well as reported by previous studies listed in the upper left corner. Yellow lines indicate major faults in the Santorini-Amorgos zone investigated by Nomikou et al. (2018). Magenta line indicates a fault imaged by Perissoratis and Papadopoulos (1999) and the orange line indicates a fault contained in GreDaSS database (Caputo and Pavlides, 2013). Inset in the lower left corresponds to profile A-B in the main figure. The solid red line on the inset represents the fault plane of AmF taken from cross-sections q-q' and r-r' of Fig. 6, while the solid magenta line indicates the location and dip of SAF. Grey shaded area represents the total thickness of the seismogenic layer. (For interpretation of the references to colour in this figure legend, the reader is referred to the web version of this article.)

Table 4

Geometrical properties of the faults in the study area. H is the thickness of seismogenic layer, L is the length of each fault, δ is the dipping angle, W is the width of the fault, A is the rupture area, and M_w is the expected moment magnitude. Asterisk symbols signify the dipping angles taken from nodal planes of available moment tensor solutions.

Fault	H (km)	L (km)	δ ($^{\circ}$)	W (km)	A (km ²)	M_w
IF	12.5	40	45	17.7	707	6.9
AF	12.5	20	45	17.7	354	6.5
AmF sc.1	12.5	40	51	16.1	643	6.8
	12.5	40	45 (*)	17.7	707	6.9
AmF sc.2	4.7	40	66	5.1	206	6.9
	7.8	40	36	13.3	531	
SAF	12.5	60	55	15.3	916	7.0
	12.5	60	37 (*)	20.8	1246	7.2
AnF	12.5	20	62	14.2	283	6.3
WAsF	12.5	30	49	16.6	331	6.4
	12.5	30	56 (*)	15.1	302	6.4
AnF-WAsF	12.5	70	55	15.3	1068	7.1
	12.5	70	56 (*)	15.1	1055	7.1
EAsF	12.5	20	45	17.7	354	6.5
LF	12.5	50	60	14.4	722	6.9

5.3. Anafi – West Astypalaia faults (AnF-WAsF)

The AnF-WAsF represents a NW dipping fault zone that extends from the west of Anafi to NW of Astypalaia and marks the SE boundary of the Santorini-Anafi basin. This fault zone consists of AnF and WAsF in its south-western and its north-eastern segments, as well as some minor faults in between. Therefore, we considered additional scenarios involving different fault segments in order to estimate the expected moment magnitude along these faults. First, we calculated the expected moment magnitude of AnF and WAsF separately. For AnF, we took the dipping angle of 62° as observed in swath bathymetry data as well as the fault length of AnF (~ 20 km) and obtained an expected moment magnitude of 6.3. As for WAsF, swath bathymetry data show a dipping angle of 45° – 53° (Nomikou et al., 2018). WAsF may also be the fault responsible for a M_w 4.5 earthquake that occurred on 10 April 2018 (Fig. 8). The moment tensor solutions of this earthquake show fault planes with dipping angles of 54° – 58° . We estimated the dipping angle of WAsF by using the median dip from bathymetry data (49°) and nodal planes in moment tensor solutions (56°). By using these median dips and the fault length of WAsF (~ 20 km), we calculated the expected moment magnitudes and both calculations resulted in a value of 6.4. After that, we consider AnF-WAsF as a single fault with a total fault length of 70

km, yielding an expected moment magnitude of 7.1.

Very little is known about the minor faults that are located between the fault segments of AnF and WASF. The only available information is that most of these faults are NW dipping with a dipping angle of $\sim 57^\circ$ as observed by Nomikou et al. (2018). A large earthquake of M_w 6.03 (± 0.4) occurred very close to this minor fault zone on 25 October 1919 (Fig. 8). The magnitude of the mentioned earthquake, however, is smaller than the expected moment magnitude of AnF-WASF if this fault ruptures along its entire length. This indicates that the 1919 earthquake might have been caused by the rupture of one of the smaller faults located between AnF and WASF. We combined various fault lengths with the observed dipping angle into eq. (2) and found that the fault which ruptured during the 1919 earthquake might have a length of 10 to 12 km.

5.4. Levitha fault (LF) and east Astypalaia fault (EAsF)

The existence of both LF and EAsF is indicated by a small number of earthquakes in the area east of Amorgos and NE of Astypalaia (Fig. 3). Based on the GreDaSS database, LF is a normal fault with SE to SSE dipping and has a dipping angle of 50° – 70° . In order to calculate the expected magnitude for this fault, we considered the median of the dipping angle and its length (~ 50 km), yielding an expected moment magnitude of 6.9. The M_w 5.50 (± 0.2) earthquake on 9 July 1956 at 20:13 UTC occurred less than 5 km from the south-western end of this fault. However, it is likely an aftershock of the 1956 twin earthquakes and is probably not related to LF. We also estimated the expected moment magnitude of EAsF which is located NE of Astypalaia and is the only fault with NW-SE orientation in the study area. Since there is no information about the dipping angle of this fault and there is no available moment tensor solution, we considered a dipping angle of 45° as it is commonly observed among normal faults. The expected moment magnitude of EAsF, if it ruptures along its entire length (~ 20 km), is 6.5.

6. Rock properties and the presence of fluids

6.1. Estimation of Vp/Vs ratio

The fact that the seismicity presented in the previous section can be correlated only with three faults (IF, AF, and AmF) signifies that the crustal earthquakes in Santorini-Amorgos zone may not be generated solely by active faulting. Crustal seismicity in this area may also be caused by upward migrating fluids that generate events with smaller magnitudes. Therefore, we estimated the spatial distribution of the Vp/Vs ratio in the Santorini-Amorgos zone and investigated its correlation with the seismic and geophysical properties of the area. Vp/Vs ratio is considered as a suitable petrophysical parameter for such an analysis due to its sensitivity to fluids, since the existence of fluid-filled cracks reduces Vs more than it reduces Vp, resulting in higher Vp/Vs ratio.

In order to estimate the distribution of Vp/Vs, we implemented the method developed by Jo and Hong (2013) that was previously used in the southern Korean peninsula and was also applied to Redoubt volcano in Alaska (Hong et al., 2014; Park et al., 2018). First, the study area was discretized into small cells with a size that allows event-station pairs to be formed. The size of these cells should be small enough so that the properties of the crust inside each cell can be assumed to be homogeneous. Therefore, we discretized the study area into cells with a size of 0.3° -by- 0.3° in latitude and longitude. Each cell overlaps with its neighboring cells by 0.27° . We selected travel times of events with hypocentral depth less than 25 km that were recorded by CYCNET, EGE-LADOS, and HUSN during our periods of study and found a total number of 14,844 P and S-travel time pairs.

The event-station travel time data were then grouped into the corresponding cells, resulting in the data density map shown in Fig. 9a. We discarded cells with less than 20 data points since their inclusion would not result in a stable estimation of the Vp/Vs ratio. Based on the number

of data points in every cell, the areas in the north to NE of Santorini and around Kolumbo submarine volcano exhibit the highest data density. The areas in the west to NE of Anydros and SW of Amorgos are also well-covered. On the other hand, the areas north of Astypalaia as well as between Paros and Naxos have lower but otherwise acceptable data density with an average of 57 data points per cell. After the discretization, we estimated the Vp/Vs ratio for each cell by using a modified Wadati method that allows us to avoid large uncertainties in the resulting Vp/Vs ratios. We constructed a least-squares line of the original dataset inside each cell and removed all outliers. An outlier is defined as any data point with travel time deviation larger than 1 s from the least-squares line. We then constructed a new least-squares line from the remaining dataset and removed newly detected outliers, as illustrated in Fig. S4 in the Supplementary Material. Usually, all the outliers will be removed after this process is repeated for 5 to 6 times. In this study we repeated the whole process for 10 times in each cell to make sure that there were no more outliers present.

The formal uncertainty of the Vp/Vs ratios can be estimated by using the bootstrap method of Efron and Tibshirani (1991). We constructed 100 samples by using random sampling with replacement to the data points of each cell. After that, we estimated the Vp/Vs ratio of each sample and calculated the standard deviation from all obtained samples. The standard deviation is then used as the uncertainty for each cell, which is found to vary from 0.002 to 0.044 throughout the study area (Fig. 9b). We next investigated the sensitivity of the Vp/Vs ratio to inaccurate origin times and phase picking errors, since both of these may cause travel time perturbations. Errors that were caused by inaccurate origin times were simulated by adding to the origin times random values between -0.5 s and 0.5 s drawn from a Gaussian distribution. The Vp/Vs ratios of the resulting dataset were then calculated and compared to the original values, yielding the distribution of Vp/Vs ratio and its difference as shown in Fig. S5 in the Supplementary Material. The Vp/Vs ratio differences are in the range of -0.029 to 0.033 with respect to the original ones. The highest absolute differences of Vp/Vs ratios of this dataset can be found between Paros and Naxos as well as in the island of Astypalaia. In a similar way, we also assessed the effect of phase picking errors by adding uniformly distributed random error to P and S-wave arrival times. We added random values of -0.1 s to 0.1 s to P-arrival times and -0.2 s to 0.2 s to S-arrival times. After the Vp/Vs ratios of this dataset were calculated and compared to the original Vp/Vs ratios, we found that the two sets have differences that range from -0.025 to 0.041 . The Vp/Vs ratios from the dataset with uniformly distributed random errors in their phases and the deviation of each cell can be seen in Fig. S6 in the Supplementary Material. The differences of Vp/Vs ratios are in the order of 0.02 to 0.04 in the areas of Astypalaia, in the south and west of Santorini, and between Paros and Naxos. We found that the Vp/Vs ratios along the Santorini-Amorgos zone are in the range of 1.69 to 2.03. High Vp/Vs ratios of 1.78–2.03 were observed between Paros and Naxos as well as in the area of Astypalaia. On the other hand, slightly lower Vp/Vs ratios (1.77–1.86) were observed in the NE end of AmF and beneath the small island of Anydros. It should be noted that the estimated Vp/Vs ratios roughly correspond to the depth of the seismogenic layer in the area.

6.2. Estimation of crack density and fluid saturation

In order to understand better how fluids affect rock properties in the Santorini-Amorgos zone, we also calculated crack density, fluid saturation, and Poisson's ratio. We utilized the model proposed by O'Connell and Budiansky (1974) which describes how seismic velocities of a solid are affected by randomly distributed circular cracks. Therefore, it is possible to connect the Vp/Vs ratios obtained previously to crack density and fluid saturation. According to this model, the total number of cracks in a partially saturated solid is defined as the sum of its dry and saturated cracks. The crack density (ϵ) of a solid can be estimated as a function of fluid saturation (ξ) defined as

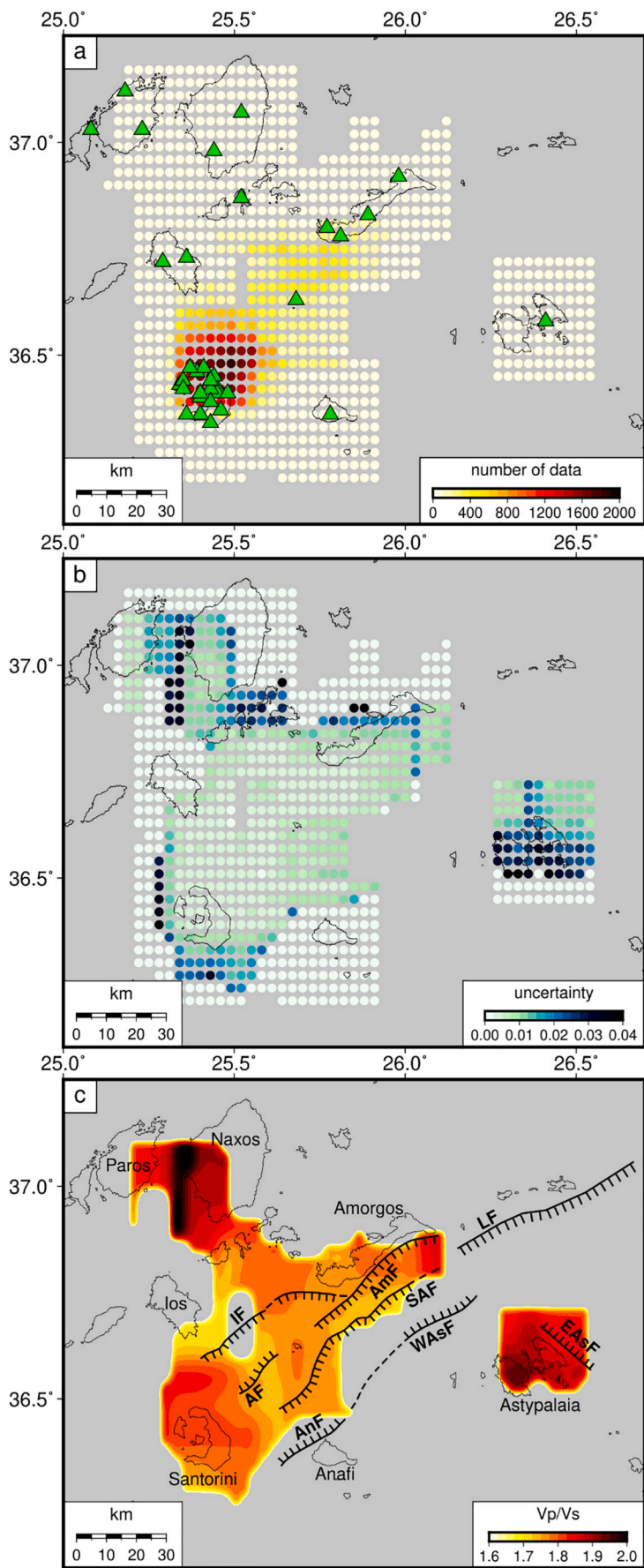


Fig. 9. Maps showing the data density, and the distribution of uncertainties as well as Vp/Vs ratios in the Santorini-Amorgos zone. (a) The number of data contained in each cell for the whole area. The total number of data of every cell varies between 1 and 1825. Green triangles represent seismic stations in the area. Maps in the lower panels show (b) the estimated Vp/Vs ratio uncertainty in every cell and (c) the spatial distribution of Vp/Vs ratio obtained by using $0.3^\circ \times 0.3^\circ$ cell that shifted by 0.03° . (For interpretation of the references to colour in this figure legend, the reader is referred to the web version of this article.)

$$\varepsilon = \frac{45}{16} \left(\frac{\nu - \bar{\nu}}{1 - \bar{\nu}^2} \right) \frac{2 - \bar{\nu}}{(1 - \xi)(1 + 3\nu)(2 - \bar{\nu}) - 2(1 - 2\nu)} \quad (3)$$

where ν and $\bar{\nu}$ are the effective Poisson's ratio for uncracked and cracked bodies, respectively. It is important to note that in a solid with dry cracks (low fluid saturation with Poisson's ratio lower than that of an uncracked solid), the value of ε cannot exceed the value of the following equation

$$\varepsilon_{\max} = \frac{9}{32} \frac{(1 + 3\bar{\nu})(2 - \bar{\nu})}{(1 - \bar{\nu}^2)} \quad (4)$$

The effective Poisson's ratio for uncracked bodies (ν) for the whole of the Santorini-Amorgos zone was calculated by utilizing the following equation

$$\nu = \frac{1}{2} \left[1 - \frac{1}{(V_p/V_s)^2 - 1} \right] \quad (5)$$

where V_p and V_s are the average of P and S-velocities of the model of [Brüster \(2012\)](#) for layers with depth between 0 and 25 km. We utilized the V_p/V_s ratios derived in the previous section to calculate the effective Poisson's ratio for cracked bodies ($\bar{\nu}$) for each cell by also using eq. (5). After all the required parameters were calculated, we estimated ε for each cell as a function of ξ by using eq. (3) and the limiting value of ε in eq. (4). The obtained values of ε and ξ in this estimation are calculated relative to the total uncracked volume, hence the maximum values of both parameters are 1. We then calculated ε for ξ ranging from 0 to 1 at an increment of 0.01, resulting in a range of values for ε and ξ . Since both parameters have the same maximum values, we only present the minimum values of ε and ξ in the following sections. The spatial distributions of minimum crack density, fluid saturation, and Poisson's ratio are plotted in [Fig. 10](#).

6.3. Interpretation of results

The estimated V_p/V_s ratios along the Santorini-Amorgos zone are in the range of 1.69 to 2.03 and their spatial distribution can be seen in [Fig. 9c](#). V_p/V_s ratios of 1.77–1.86 are observed beneath the small island of Anydros and in the NE end of AmF, where vertical earthquake clusters have been observed. Such structures may be related to fluid-extraction or degassing from the sea floor as proposed previously by [Bohnhoff et al. \(2006\)](#) which is compatible with the high V_p/V_s ratios observed here. Higher V_p/V_s ratios (1.78–2.03) were observed between Paros and Naxos as well as in the area of Astypalaia (1.81–1.95). Considering that the uncertainties found in the mentioned areas are also high ([Fig. 9b](#)), it is likely that the estimated V_p/V_s ratios in these areas are not accurate enough.

The V_p/V_s ratios around the Santorini caldera are found to vary from 1.74 to 1.91. A more careful look reveals that high V_p/V_s ratios can be found in the northern part of Santorini caldera, extending northward to NE of the caldera. Low velocity anomalies have also been observed in the northern part of Santorini caldera with NE-SW orientation ([Heath et al., 2019](#); [Hooft et al., 2019](#)). Similarly, recent P-wave tomography by [McVey et al. \(2020\)](#) revealed the existence of a magma body containing 11%–30% of melt at the depths of 2.8–5 km beneath the same location which agrees well with the high V_p/V_s ratios shown here. Moreover, the authors also highlighted the NE-SW oriented low velocity region beneath Santorini caldera. This region is interpreted as mush with 3%–10% of melt at depths of 2.8–5 km. Interestingly, the same studies indicate that only up to 1% of melt could be resolved beneath Kolumbo even though there is a strong possibility of a magma chamber located at the depth of 6–7 km (see inset of cross-section g-g' in [Fig. 5](#)) as discussed in the previous section.

The northern part of Santorini caldera as well as the area to its north exhibit crack density in the range of 0.05 to 0.35 with high fluid saturation of 0.68–0.77. These values are consistent with the obtained V_p/V_s

ratios (1.74–1.91) and the existence of a magma body in the area. High values of crack density (0.15–0.30) and fluid saturation (0.71–0.76) can also be found in the NE end of AmF where a vertical earthquake cluster was observed. Lower crack density (0.10–0.15) but high fluid saturation of 0.70–0.71 are found around the small island of Anydros, where a similar vertical cluster can be seen.

The offshore area between Santorini and Amorgos exhibits low crack density values of 0.10–0.20 and fluid saturation of 0.65–0.72. Low crack density in this area may indicate the presence of cracks that concentrate along the damage zone of the active faults, which results in a lower fluid saturation away from these faults. The existence of these concentrated cracks along the fault damage zones is not enough to create a visible increase in the V_p/V_s ratios since the damage zones have probably small widths in the order of hundreds of meters. Hence, we also observe slightly lower V_p/V_s ratios in the area between Santorini and Amorgos (see [Fig. 9c](#)).

The Poisson's ratios of the whole study area vary between 0.23 and 0.34 and its distribution is plotted in [Fig. 10c](#). Lower Poisson's ratios are only observed south of Amorgos and in between the island of Ios and IF, while relatively high Poisson's ratios of 0.25–0.31 are observed to the north of Santorini and near the NE end of AmF. These areas are most likely related to extensive magmatic intrusions and high fluid saturation. A fully saturated solid will exhibit decreased S-velocities which leads to a high Poisson's ratio of ~ 0.5 (see Eq. 5). Hence, a solid with partially saturated cracks will have a relatively higher Poisson's ratio than one with dry cracks. The fact that the observed Poisson's ratios are higher than 0.25 indicates that the Santorini-Amorgos zone is mostly characterized by rocks with partially saturated cracks.

7. Conclusions

We obtained 1455 precise relative locations of crustal events along the Santorini-Amorgos zone recorded by both temporary and permanent networks and used these locations to better understand the active tectonics of the area. The conclusions of our study are as follows:

- The relocated seismicity has horizontal and vertical uncertainties of less than 0.3 km and clearly delineated three (AF, IF, and AmF) of the eight faults in the study area. Other than that, the relocated seismicity also revealed vertical clusters of hypocenters, such as beneath the island of Anydros, south of Amorgos, and in the NE end of AmF, indicating the possible involvement of upward migrating fluids.
- The seismogenic layer of the Santorini-Amorgos zone was found to be 12.5 km thick. The maximum expected moment magnitudes of future earthquakes range between 6.3 and 7.2 with SAF having the largest expected moment magnitudes (7.0–7.2). It is possible that one of these faults may rupture and generate a large earthquake followed by a tsunami since all of them have expected moment magnitude close to 7.0 (i.e. IF, AmF, SAF, AnF-WAsF, LF). Moreover, the area is a popular tourist destination that attracts hundreds of thousands of people every year, which increases its vulnerability to both seismic and tsunami hazards.
- The V_p/V_s ratios observed between Santorini and Amorgos (1.77–1.86) indicate the presence of cracks concentrated along the damage zone of the active faults which results in lower crack density and fluid saturation away from the faults. Crustal seismicity distribution and petrophysical parameters strongly suggest the existence of melt in the northern part of the Santorini caldera and also upward migrating fluids beneath the island of Anydros as well as in the NE end of AmF.

Supplementary data to this article can be found online at <https://doi.org/10.1016/j.pepi.2021.106660>.

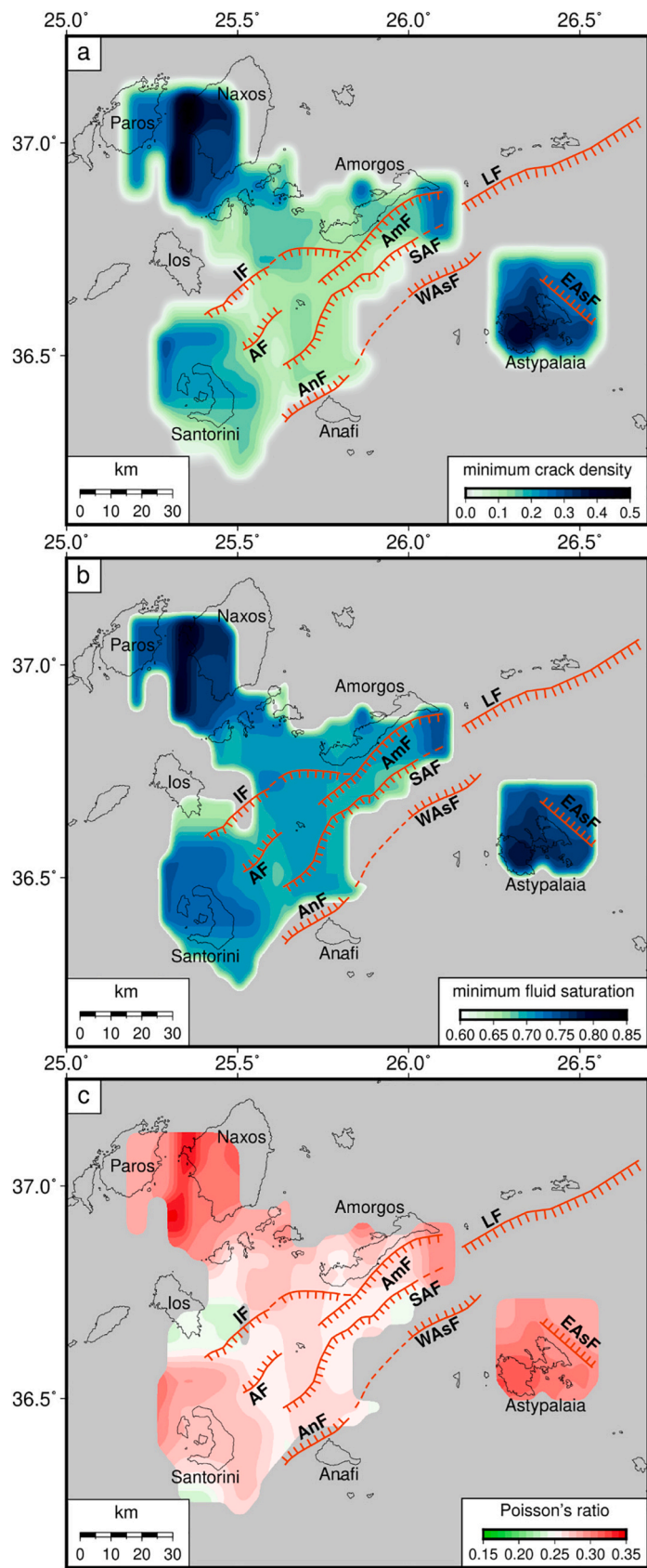


Fig. 10. Variation of rock properties along the Santorini-Amorgos zone. Maps of (a) minimum crack density, (b) minimum fluid saturation calculated by using the model of O'Connell and Budiansky (1974), and also (c) map showing the resulting Poisson's ratio.

Declaration of Competing Interest

The authors declare that they have no known competing financial interests or personal relationships that could have appeared to influence the work reported in this paper.

Acknowledgments

This research has been funded by a scholarship from the National Central University (NCU) School of Earth Sciences (R. Andinisari), a Ministry of Science and Technology of Taiwan (MOST) grant (K.I. Konstantinou), and also a Taiwan International Graduate Program (TIGP) scholarship (P. Ranjan). The waveforms recorded by CYCNET can be downloaded from FDSNWS DataSelect Web Service (<http://geo.n.gfz-potsdam.de/fdsnws/dataselect/1/>). The waveforms recorded by EGELADOS can be downloaded from GFZ, Postdam, European Integrated Data Archive (EIDA) website (<http://eida.gfz-postdam.de/webdc3>) with the network code Z3. The waveforms recorded by HUSN can be downloaded from the National Observatory of Athens, EIDA archives with the network code HUSN (<http://eida.gein.noa.gr/webdc3>). The moment tensor solutions used in this study can be found in the RCMT database (<http://rcmt2.bo.ingv.it>) and the database of National Observatory of Athens, Institute of Geodynamics (<http://bbnet.gein.noa.gr>). We would like to thank Frederik Tilmann for allowing us to use his waveform cross-correlation code. We would also like to thank the editor Mark Jellinek, as well as Marco Bohnhoff and an anonymous reviewer for their constructive comments.

References

- Ambraseys, N., 1960. The seismic sea wave of July 9, 1956, in the Greek archipelago. *J. Geophys. Res.* 65, 1257–1265. <https://doi.org/10.1029/JZ065i004p01257>.
- Ambraseys, N., 2001. Reassessment of earthquakes, 1900–1999, in the Eastern Mediterranean and the Middle East. *Geophys. J. Int.*, 145 471–485. <https://doi.org/10.1046/j.0956-540x.2001.01396.x>.
- Andinisari, R., Konstantinou, K.I., Ranjan, P., 2020. Seismotectonics of SE Aegean inferred from precise relative locations of shallow crustal earthquakes. *J. Seismol.* 24, 1–22. <https://doi.org/10.1007/s10950-019-09881-8>.
- Bohnhoff, M., Rische, M., Meier, T., Endrun, B., Harjes, H.-P., Stavrakakis, G., 2004. A temporary seismic network on the Cyclades (Aegean Sea, Greece). *Seismol. Res. Lett.* 75 (3), 352–357. <https://doi.org/10.1785/gssrl.75.3.352>.
- Bohnhoff, M., Rische, M., Meier, T., Becker, D., Stavrakakis, G., Harjes, H.P., 2006. Microseismic activity in the Hellenic volcanic arc, Greece, with emphasis on the seismotectonic setting of the Santorini-Amorgos zone. *Tectonophysics* 423 (1–4), 17–33. <https://doi.org/10.1016/j.tecto.2006.03.024>.
- Brüster, A., 2012. Seismicity of the eastern Hellenic Subduction Zone. Ph.D. thesis. Ruhr University, Bochum.
- Brüster, A., Friederich, W., Meier, T., Gross, C., 2014. Focal mechanism and depth of the 1956 Amorgos twin earthquakes from waveform matching of analogue seismograms. *Solid Earth* 5, 1027–1044. <https://doi.org/10.5194/se-5-1027-2014>.
- Caputo, R., Pavlides, S., 2013. The Greek Database of Seismogenic Sources (GreDaSS), Version 2.0.0: a Compilation of Potential Seismogenic Sources (Mw & 5.5) in the Aegean Region. <https://doi.org/10.15160/unife/gredass/0200>. <http://gredass.unife.it/>.
- Collettini, C., Sibson, R.H., 2001. Normal faults, normal friction? *Geology* 29 (10), 927–930. [https://doi.org/10.1130/0091-7613\(2001\)029<0927:NFNF>2.0.CO;2](https://doi.org/10.1130/0091-7613(2001)029<0927:NFNF>2.0.CO;2).
- Comninakis, P., Papazachos, B., 1986. A Catalogue of Earthquakes in Greece and the Surrounding Area for the Period 1901–1985. Univ. Thessaloniki Geophys. Lab. Publ.
- Corti, G., Bonini, M., Conticelli, S., Innocenti, F., Manetti, P., Sokoutis, D., 2003. Analogue modelling of continental extension: a review focused on the relations between the patterns of deformation and the presence of magma. *Earth Sci. Rev.* 63 (3–4), 169–247. [https://doi.org/10.1016/S0012-8252\(03\)00035-7](https://doi.org/10.1016/S0012-8252(03)00035-7).
- Dimitriadis, I., Karagianni, E., Panagiotopoulos, D., Papazachos, C., Hatzidimitriou, P., Bohnhoff, M., Rische, M., Meier, T., 2009. Seismicity and active tectonics at Coloumbo Reef (Aegean Sea, Greece): monitoring an active volcano at Santorini Volcanic Center using a temporary seismic network. *Tectonophysics* 465 (1–4), 136–149. <https://doi.org/10.1016/j.tecto.2008.11.005>.
- Dimitriadis, I., Papazachos, C., Panagiotopoulos, D., Hatzidimitriou, P., Bohnhoff, M., Rische, M., Meier, T., 2010. P and S velocity structures of the Santorini-Coloumbo volcanic system (Aegean Sea, Greece) obtained by non-linear inversion of travel times and its tectonic implications. *J. Volcanol. Geotherm. Res.* 195 (1), 13–30. <https://doi.org/10.1016/j.jvolgeores.2010.05.013>.
- Druitt, T.H., Pyle, D.M., Mather, T.A., 2019. Santorini volcano and its plumbing system. *Elements* 15 (3), 177–184. <https://doi.org/10.2138/gselements.15.3.177>.
- Efron, B., Tibshirani, R., 1991. Statistical data analysis in the computer age. *Science* 253, 390–395. <https://doi.org/10.1126/science.253.5018.390>.
- Friederich, W., Meier, T., 2005. EGELADOS project 2005/07, RUB Bochum, Germany. Deutsches GeoForschungsZentrum GFZ. <https://doi.org/10.14470/m87550267382>.
- Friedrich, W.L., 2013. The Minoan eruption of santorini around 1613 B.C. and its consequences. *Tagungen des Landesmuseums für Vorgeschichte Halle* 9, 37–48.
- Heath, B.A., Hooff, E.E.E., Toomey, D.R., Papazachos, C.B., Nomikou, P., Paulatto, M., et al., 2019. Tectonism and its relation to magmatism around Santorini volcano from upper crustal Pwave velocity. *J. Geophys. Res. Solid Earth* 124 (10), 610, 629. <https://doi.org/10.1029/2019JB01769910>.
- Hollenstein, C., Müller, M.D., Geiger, A., Kahle, H.-G., 2008. Crustal motion and deformation in Greece from a decade of GPS measurements, 1993–2003. *Tectonophysics* 449 (1), 17–40. <https://doi.org/10.1016/j.tecto.2007.12.006>.
- Hong, T.-K., Hough, S.E., Jo, E., 2014. Temporal changes of medium properties during explosive volcanic eruption. *Geophys. Res. Lett.* 41, 1944–1950. <https://doi.org/10.1002/2014GL059408>.
- Hooff, E.E.E., Heath, B.A., Toomey, D.R., Paulatto, M., Papazachos, C.B., Nomikou, P., et al., 2019. Seismic imaging of Santorini: subsurface constraints on caldera collapse and present-day magma recharge. *Earth Planet. Sci. Lett.* 514, 48–61. <https://doi.org/10.1016/j.epsl.2019.02.033>.
- Jo, E., Hong, T.K., 2013. VP/VS ratios in the upper crust of the southern Korean peninsula and their correlations with seismic and geophysical properties. *J. Asian Earth Sci.* 66, 204–214. <https://doi.org/10.1016/j.jseaes.2013.01.008>.
- Klaver, M., Carey, S., Nomikou, P., Smet, I., Godelitsas, A., Vroon, P., 2016. A distinct source and differentiation history for Kolumbo submarine volcano, Santorini volcanic field, Aegean arc. *Geochim. Geophys. Geosyst.* 17, 3254–3273. <https://doi.org/10.1002/2016GC006398>.
- Konstantinou, K.I., 2010. Crustal rheology of the Santorini–Amorgos zone: implications for the nucleation depth and rupture extent of the 9 July 1956 Amorgos earthquake, southern Aegean. *J. Geodyn.* 50 (5), 400–409. <https://doi.org/10.1016/j.jog.2010.05.002>.
- Konstantinou, K.I., 2014. Moment magnitude-rupture area scaling and stress-drop variations for earthquakes in the Mediterranean region. *Bull. Seismol. Soc. Am.* 104 (5), 2378. <https://doi.org/10.1785/0120140062>.
- Konstantinou, K.I., 2018. Estimation of optimum velocity model and precise earthquake locations in NE Aegean: implications for seismotectonics and seismic hazard. *J. Geodyn.* 121, 143–154. <https://doi.org/10.1016/j.jog.2018.07.005>.
- Konstantinou, K.I., 2020. Magma chamber evolution during the 1650 AD Kolumbo eruption provides clues about past and future volcanic activity. *Sci. Rep.* 10, 15423. <https://doi.org/10.1038/s41598-020-71991-y>.
- Konstantinou, K.I., Melis, N.S., Boukouras, K., 2010. Routine regional moment tensor inversion for earthquakes in the Greek region: the National Observatory of Athens (NOA) Database (2001–2006). *Seismol. Res. Lett.* 81, 750–760. <https://doi.org/10.1785/gssrl.81.5.750>.
- Konstantinou, K.I., Evangelidis, C.P., Liang, W.-T., Melis, N.S., Kalogeras, I., 2013. Seismicity, Vp/Vs and shear wave anisotropy variations during the 2011 unrest at Santorini caldera, southern Aegean. *J. Volcanol. Geotherm. Res.* 267, 57–67. <https://doi.org/10.1016/j.jvolgeores.2013.10.001>.
- Konstantinou, K.I., Mouslopoulou, V., Liang, W.-T., Heidbach, O., Oncken, O., Suppe, J., 2016. Present-day crustal stress field in Greece inferred from regional-scale damped inversion of earthquake focal mechanisms. *J. Geophys. Res. Solid Earth* 122, 506–523. <https://doi.org/10.1002/2016JB013272>.
- Le Pichon, X., Chamot-Rooke, N., Lallemand, S., Noomen, R., Veis, G., 1995. Geodetic determination of the kinematics of Central Greece with respect to Europe: implications for eastern Mediterranean tectonics. *J. Geophys. Res.* 100 (B7), 12,675–12,690. <https://doi.org/10.1029/95JB00317>.
- Lomax, A., Virieux, J., Volcant, P., Thierry-Berge, C., (2000). Probabilistic earthquake location in 3D and layered models, in *Advances in Seismic Events Location*. 101–134 pp. Thurber, C. H., Rabinowitz, N. (eds), Amsterdam.
- Makropoulos, K., Drakopoulos, J., Latousakis, J., 1999. A revised and extended earthquake catalogue for Greece since 1900. *Geophys. J. Int.* 98, 391–394. <https://doi.org/10.1111/j.1365-246X.1999.tb03360.x>.
- Maleki, V., Hosseini Shomali, Z., Hatami, M.R., Pakzad, M., Lomax, A., 2013. Earthquake relocation in the central Alborz region of Iran using a nonlinear probabilistic method. *J. Seismol.* 17, 615–628. <https://doi.org/10.1007/s10950-012-9342-3>.
- McClusky, S., Balassanian, S., Barka, A., Demir, C., Ergintav, S., Georgiev, I., Gurkan, O., Hamburger, M., Hurst, K., Kahle, H., Kastens, K., Kekelidze, G., King, R., Kotzev, V., Lenk, O., Mahmoud, S., Mishin, A., Nadariya, M., Ouzounis, A., Paradisis, D., Peter, Y., Prilepin, M., Reilinger, R., Sanli, I., Seeger, H., Tealeb, A., Toksöz, M.N., Veis, G., 2000. Global positioning system constraints on plate kinematic and dynamics in the eastern Mediterranean and Caucasus. *J. Geophys. Res.* 105, 5695–5719. <https://doi.org/10.1029/1999JB900351>.
- McVey, B.G., Hooff, E.E.E., Heath, B.A., Toomey, D.R., Paulatto, M., Morgan, J.V., Nomikou, P., Papazachos, C.B., 2020. Magma accumulation beneath Santorini volcano, Greece, from P-wave tomography. *Geology* 48 (3), 231–235. <https://doi.org/10.1130/G47127.1>.
- Newman, A.V., Stiros, S., Feng, L., Psimoulis, P., Moschas, F., Saltogianni, V., Jiang, Y., Papazachos, C., Panagiotopoulos, D., Karagianni, E., Vamvakaris, D., 2012. Recent geodetic unrest at Santorini Caldera, Greece. *Geophys. Res. Lett.* 39, L06309. <https://doi.org/10.1029/2012GL051286>.
- Nomikou, P., Carey, S., Papanikolaou, D., Croff Bell, K., Sakellariou, D., Alexandri, M., Bejelou, K., 2012. Submarine volcanoes of the Kolumbo volcanic zone NE of Santorini Caldera, Greece. *Glob. Planet. Chang.* 90–91, 135–151. <https://doi.org/10.1016/j.gloplacha.2012.01.001>.
- Nomikou, P., Papanikolaou, D., Pyle, D.M., Mather, T.A., Carey, S., Watts, A.B., Paulatto, M., Kalnins, M.L., Livanos, I., Bejelou, K., Simou, E., Perros, I., 2014. The emergence and growth of a submarine volcano: the Kameni islands, Santorini (Greece). *GeoResJ* 1–2, 8–18. <https://doi.org/10.1016/j.grj.2014.02.002>.

- Nomikou, P., Hübscher, C., Ruhnu, M., Bejelou, K., 2016. Tectono-stratigraphic evolution through successive extensional events of the Anydros Basin, hosting Kolumbo volcanic field at the Aegean Sea, Greece. *Tectonophysics* 671, 202–217. <https://doi.org/10.1016/j.tecto.2016.01.021>.
- Nomikou, P., Hübscher, C., Papanikolaou, D., Farangitakis, G.P., Ruhnu, M., Lampridou, D., 2018. Expanding extension, subsidence and lateral segmentation within the Santorini - Amorgos basins during quaternary: implications for the 1956 Amorgos events, central - South Aegean Sea, Greece. *Tectonophysics* 722, 138–153. <https://doi.org/10.1016/j.tecto.2017.10.016>.
- Nyst, M., Thatcher, W., 2004. New constraints on the active tectonic deformation of the Aegean. *J. Geophys. Res.* 109, B11406 <https://doi.org/10.1029/2003JB002830>.
- O'Connell, R.J., Budiansky, B., 1974. Seismic velocities in dry and saturated cracked solids. *J. Geophys. Res.* 79 (35), 5412–5426. <https://doi.org/10.1029/JB079i035p05412>.
- Okal, E., Synolakis, C., Uslu, B., Kalligeris, N., Voukouvalas, E., 2009. The 1956 earthquake and tsunami in Amorgos, Greece. *Geophys. J. Int.* 178, 1533–1554. <https://doi.org/10.1111/j.1365-246X.2009.04237.x>.
- Papazachos, B.C., Karakostas, V.G., Papazachos, C.B., Scordilis, E.M., 2000. The geometry of the Wadati-Benioff zone and lithospheric kinematics in the Hellenic arc. *Tectonophysics* 275–300. [https://doi.org/10.1016/S0040-1951\(99\)00299-1](https://doi.org/10.1016/S0040-1951(99)00299-1).
- Papazachos, B.C., Koutitas, C., Hatzidimitriou, P.M., Karakostas, B.G., Papaioannou, C. A., 1985. Source and short-distance propagation of the July 9, 1956 southern Aegean tsunami. *Mar. Geol.* 65, 343–353. [https://doi.org/10.1016/0025-3227\(85\)90064-7](https://doi.org/10.1016/0025-3227(85)90064-7).
- Park, S., Hong, T.K., Buurman, H., 2018. Temporal change of upper-crustal Vp/Vs ratios with volcanic evolution in Redoubt Volcano. *Phys. Earth Planet. Inter.* 282, 39–48. <https://doi.org/10.1016/j.pepi.2018.07.003>.
- Parks, M.M., Moore, J.D.P., Papanikolaou, X., Biggs, J., Mather, T.A., Pyle, D.M., Raptakis, C., Paradissis, D., Hooper, A., Parsons, B., Nomikou, P., 2015. From quiescence to unrest: 20 years of satellite geodetic measurements at Santorini volcano, Greece. *J. Geophys. Res. Solid Earth* 120, 1309–1328. <https://doi.org/10.1002/2014JB011540>.
- Perissoratis, C., Papadopoulos, G., 1999. Sediment instability and slumping in the southern Aegean Sea and the case history of the 1956 tsunami. *Mar. Geol.* 161, 287–305. [https://doi.org/10.1016/S0025-3227\(99\)00039-0](https://doi.org/10.1016/S0025-3227(99)00039-0).
- Podvin, P., Lecomte, I., 1991. Finite difference computation of traveltimes in very contrasted velocity models: a massively parallel approach and its associated tools. *Geophys. J. Int.* 105, 271–284. <https://doi.org/10.1111/j.1365-246X.1991.tb03461.x>.
- Ranjan, P., Konstantinou, K.I., Andinisari, R., 2019. Spatial distribution of random velocity inhomogeneities in the southern Aegean from inversion of S wave peak delay times. *J. Geophys. Res. Solid Earth* 124, 10393–10412. <https://doi.org/10.1029/2018JB017198>.
- Reillinger, R., McClusky, S., Vernant, P., Lawrence, S., Ergintav, S., Cakmak, R., Ozener, H., Kadirov, F., Guliev, I., Stepanyan, R., Nadariya, M., Hahubia, G., Mahmoud, S., Sakr, K., ArRajehi, A., Paradissis, D., Al-Aydrus, A., Prilepin, M., Guseva, T., Evren, E., Dmitrova, A., Filikov, S.V., Gomez, F., Al-Ghazzi, R., Karam, G., 2006. GPS constraints on continental deformation in the Africa–Arabia–Eurasia continental collision zone and implications for the dynamics of plate interactions. *J. Geophys. Res.* 111 <https://doi.org/10.1029/2005JB004051>.
- Rontogianni, S., 2010. Comparison of geodetic and seismic strain rates in Greece by using a uniform processing approach to campaign GPS measurements over the interval 1994–2000. *J. Geodyn.* 50, 381–399. <https://doi.org/10.1016/j.jog.2010.04.008>.
- Sakellariou, D., Sigurdsson, H., Alexandri, M., Carey, S., Rousakis, G., Nomikou, P., Georgiou, P., Ballas, D., 2010. Active tectonics in the Hellenic volcanic arc: The Kolumbo submarine volcanic zone. *Bull. Geol. Soc. Greece* 43 (2), 1056–1063. <https://doi.org/10.12681/bgsg.11270>.
- Sibson, R.H., 1984. Roughness at the base of the seismogenic zone: contributing factors. *J. Geophys. Res.* 89 (B7), 5791–5799. <https://doi.org/10.1029/JB089iB07p05791>.
- Storchak, D.A., Di Giacomo, D., Bondár, I., Engdahl, E.R., Harris, J., Lee, W.H.K., Villaseñor, A., Bormann, P., 2013. Public release of the ISC-GEM global instrumental earthquake catalogue (1900–2009). *Seismol. Res. Lett.* 84 (5), 810–815. <https://doi.org/10.1785/0220130034>.
- VanDecar, J.C., Crosson, R.S., 1990. Determination of teleseismic relative phase arrival times using multi-channel cross-correlation and least squares. *Bull. Seismol. Soc. Am.* 80 (1), 150–169.
- Waldhauser, F., 2001. HypoDD: a computer program to compute double-difference earthquake locations. *USGS Open File Rep.* 01-113, 2001.
- Waldhauser, F., Ellsworth, W.L., 2000. A double-difference earthquake location algorithm: method and application to the northern Hayward fault. *Bull. Seismol. Soc. Am.* 90, 1353–1368. <https://doi.org/10.1785/0120000006>.
- Weatherall, P., Marks, K.M., Jakobsson, M., Schmitt, T., Tani, S., Arndt, J.E., Rovere, M., Chayes, D., Ferrini, V., Wigley, R., 2015. A new digital bathymetric model of the world's oceans. *Earth Space Sci.* 2, 331–345. <https://doi.org/10.1002/2015EA000107>.